JOURNAL OF GEOPHYSICAL RESEARCH, VOL. 95, NO. D4, PAGES 3659-3686, MARCH 20, 1990

Aerosol Size Distributions and Optical Properties Found in the Marine Boundary Layer Over the Atlantic Ocean

W. A. HOPPEL, J. W. FITZGERALD, G. M. FRICK, AND R. E. LARSON

Atmospheric Physics Branch, Space Science Division, Naval Research Laboratory, Washington, D. C.

E. J. MACK[1]

Advance Technology Center, Arvin Calspan Corporation, Buffalo, New York

Measurements and analyses of the aerosol size distributions and optical properties found in the marine boundary layer (MBL) during the 1983 USNS *Lynch* cruise from Charleston, South Carolina, to Scotland via Canary Islands are presented. The data given are the most extensive and accurate measurements of the submicron marine aerosol size distribution to date and are supplemented by extensive meteorological observations. Eight detailed case studies of the evolution of the size distribution that occurred under different meteorological conditions are presented and discussed. The data indicate that repeated cycling of MBL air through nonprecipitating clouds at the top of the MBL is a major factor in shaping the size distribution and that new particle formation by heteromolecular, homogeneous nucleation is the most likely mechanism for sustaining the particle concentration below 0.04-μm radius. Calculations of the scattering and extinction coefficients and optical depth of the MBL as a function of wavelength directly from the measured size distribution and MBL vertical structure are compared to measured values of the scattering coefficient and optical depth. These measured and calculated optical properties correlate well throughout the cruise and the results give a relatively consistent picture of the relationship between the aerosol size distribution and electromagnetic properties in the MBL.

1. INTRODUCTION

Atmospheric aerosols impact a number of disciplines within the atmospheric sciences: (1) They provide the nucleation sites on which cloud and fog droplets form and therefore determine the microphysical and optical properties of clouds. (2) They affect solar radiative transfer directly and through their influence on cloud albedo and hence are important in climate studies. (3) Aerosols are intimately related to atmospheric chemistry since many trace gases pass through the particulate phase before being removed by precipitation scavenging. (4) Lidar remote sensing depends upon the backscatter off aerosols for the return signal. (5) Electromagnetic extinction due to aerosols affects visibility and military surveillance systems. The large number of submicron particles associated with urban pollution episodes and their relation to public health and welfare have resulted in a significant effort to study submicron particles in the urban environment and their relationship to air chemistry. There has been no comparable effort in the marine environment. Most efforts in the marine environment have been concerned with the larger sea-salt particles generated at the sea surface or dust particles from the world's deserts.

This study was designed to investigate marine aerosols with emphasis on submicron particles. It is a continuation of the aerosol measurements made at a coastal site along the east coast of the United States [*Hoppel et al.*, 1984] and shipboard measurements in air masses advecting off the east coast of the United States [*Hoppel et al.*, 1983, 1985]. These prior measurements which were made primarily in air masses dominated by continental influences have provided an excellent data set with which to contrast the aerosol found during our more recent cruises in the remote tropical Atlantic and Pacific.

The data presented in this report were taken during a transatlantic cruise aboard the USNS *Lynch* in March and April of 1983. The cruise was dedicated to aerosol and marine boundary layer research and involved personnel from several institutions. This report deals primarily with measurements and interpretation of the aerosol size distribution and aerosol optical effects, including a comparison of measured optical properties with those calculated from aerosol data. In addition to the aerosol size distribution data, extensive use is made of the local meteorological and satellite observations, balloon soundings of temperature and relative humidity, aerosol chemistry, and air mass trajectory analyses.

2. OVERVIEW OF CRUISE

The USNS Lynch sailed from Charleston, South Carolina, on March 11, 1983, and followed the track shown in Figure 1, across the tropical North Atlantic to the Canary Islands. After 8 days in port at Las Palmas the cruise continued on to Scotland, arriving there on April 17.

The data presented in this report were obtained with the following instrumentation: (1) Aerosol size distributions were measured with the Naval Research Laboratory (NRL) differential mobility analyzer (DMA) [*Hoppel et al.*, 1983], which covered the size range from 0.006- to 0.5-μm radius, and with the Calspan impactor [*Mack et al.*, 1980] in the range of 0.5–50 μm. Data from two Particle Measuring Systems Company (PMS) optical counters and a Thermal

[1]Deceased October 18, 1986.

Paper number 89JD02981.

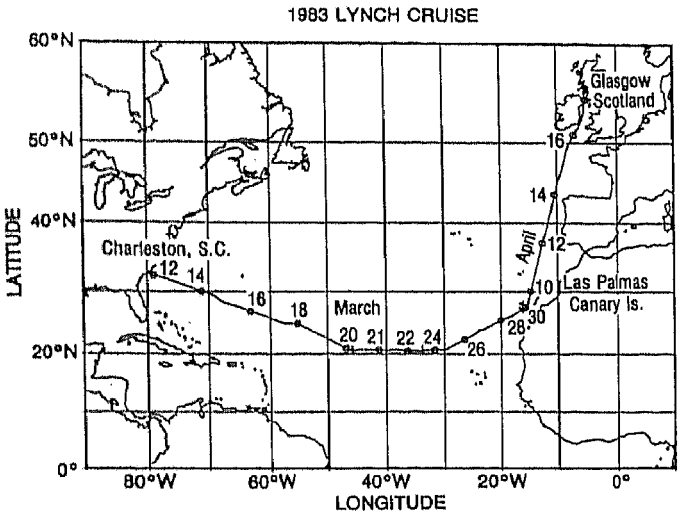

Fig. 1. Map showing the 1983 *Lynch* cruise track.

Systems Electrical Aerosol Analyzer (EEA) were available but not used in this analysis for reasons cited by *Hoppel et al.* [1989]. (2) The scattering coefficient was measured with an Meteorology Research, Inc. (MRI) integrating nephelometer and an HSS, Inc. visiometer. (3) Radon 222 was measured with the NRL radon monitor [*Larson*, 1973]. (4) Optical depth was measured with a Volz multiwavelength sun photometer. (5) Total aerosol concentrations (Aitken nuclei) were measured hourly with a Gardner counter. The instrumentation was mounted in a shelter on the bow of the ship, and the air samples, except for the Calspan impactor, were taken from about 5 m above the bow deck at a total height of about 11 m. The impactor data were taken from the forwardmost point of the bow at about 6.7 m above the sea surface. Ten-day back trajectories of the air arriving at the ship were calculated using the computer model described by *Harris* [1982]. More detailed information on the instrumentation and comparison of measurements is provided by *Hoppel et al.* [1989].

The size distributions given in this report contain three corrections which were not made in our earlier papers. (1) Subsequent to the cruise, the diffusion loss in the DMA and neutralizer was measured, and a small correction in our raw data was made to account for diffusive loss. (2) An extensive study [*Hoppel and Frick*, 1990] of the nonsymmmetric charging characteristics of neutralizers showed that the ratio of negatively charged particles to positively charged particles was about 1.3 for the neutralizer used in this study. Since positively charged particles were measured in the DMA, this means that the raw counts were about 15% below the mean of the positive and negative concentrations. We further corrected our raw counts by this factor. (3) The corrected raw data were then used to recalculate all the size distributions taken on our 1983 cruise. The inversion scheme now uses the charge distribution published by *Hoppel and Frick* [1986] for symmetric charging with 150 amu ions. (The nonsymmetric nature of the charge was accounted for in correction 2 above.) In our earlier papers the size distribution had been calculated from the DMA data assuming that the aerosol had a Boltzmann charge distribution. The net effect of these corrections on the calculated size distribution was to increase the number of particles in the seven largest size channels ($r > 0.015$ μm) by 4–25% and to decrease the concentrations in the smallest three channels ($r = 0.013$, 0.009, and 0.006 μm) by factors of 1.2, 1.8, and 3.6. (The large corrections in the smallest two channels reflect the large departure of the true charge distribution from the Boltzmann distribution at small radii.)

2.1. *Chronological Displays of Selected Data*

A chronological display of selected data throughout the cruise is shown in Figures 2–6. The ship's location corre-

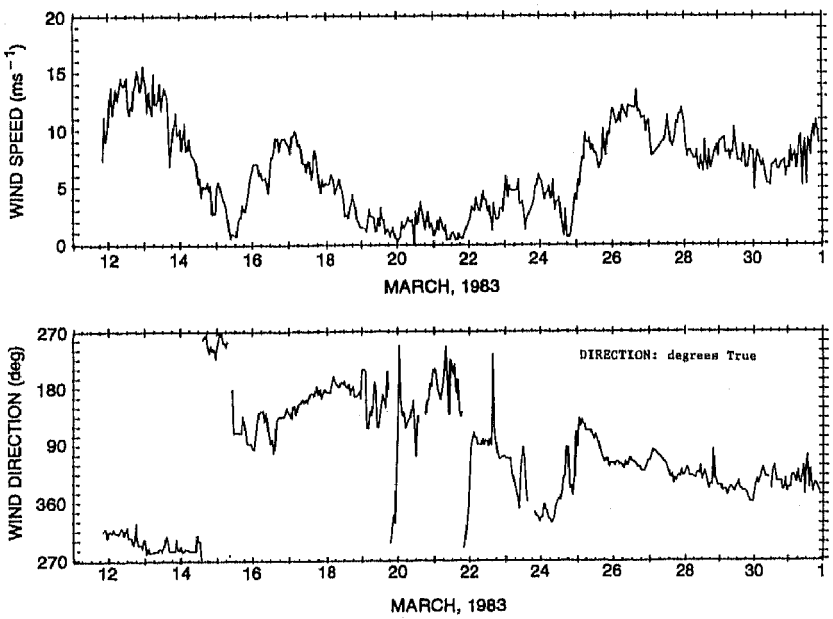

Fig. 2. Chronological history of wind speed and direction for the Charleston, South Carolina, to Canary Islands leg of the cruise.

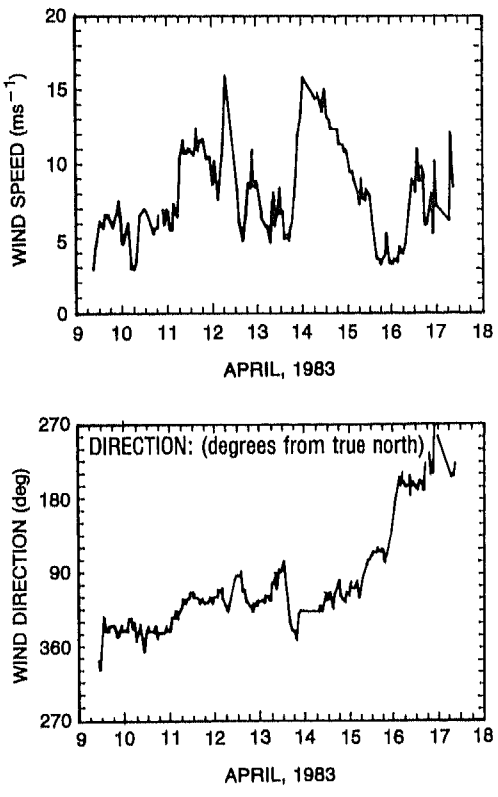

Fig. 3. Chronological history of wind speed and direction for the Canary Islands to Scotland leg of the cruise.

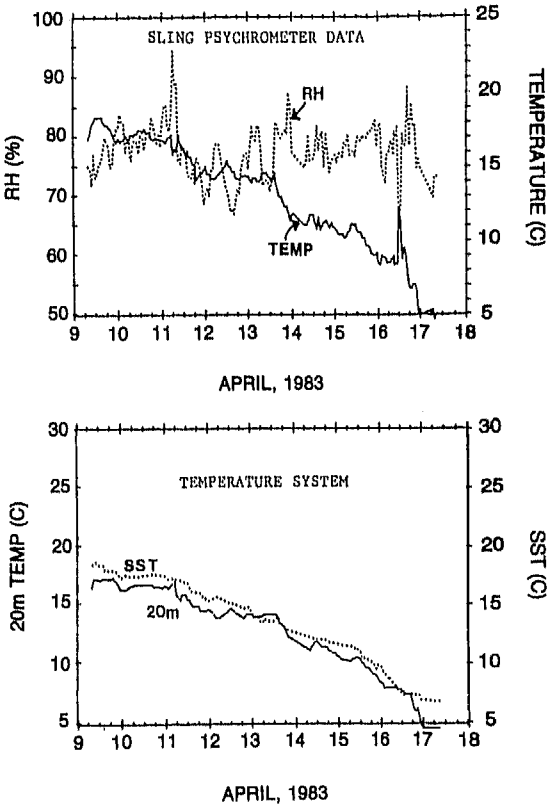

Fig. 5. Chronological history of air temperature and relative humidity at deck height, the sea surface temperature, and air temperature at 20 m for the Canary Islands to Scotland leg of the cruise.

sponding to a given time can be obtained from Figure 1. Figures 2 and 3 show the wind speed and direction on the two legs of the cruise. Absolute wind speed and direction were calculated from the ship's velocity and the relative wind speed and direction measured at the 20-m height on the mast with the Beckmann-Whitley wind system. The temperature and relative humidity, shown in Figures 4 and 5, were taken hourly on the bow of the ship with a sling psychrometer. Also shown are the sea surface temperature taken every 2 hours via bucket samples and the temperature at 20 m above the sea surface. Figure 6 shows the radon concen-

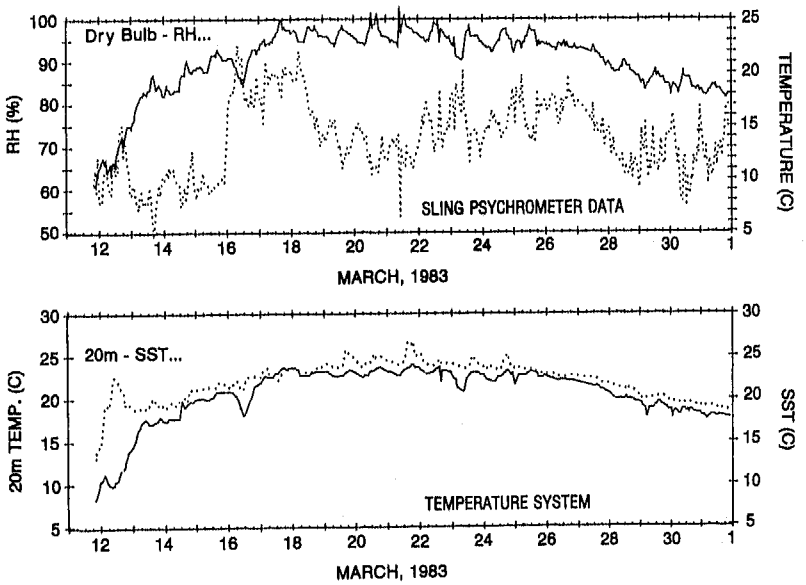

Fig. 4. Chronological history of air temperature and relative humidity at deck height, the sea surface temperature, and air temperature at 20 m for the Charleston, South Carolina, to Canary Islands leg of the cruise.

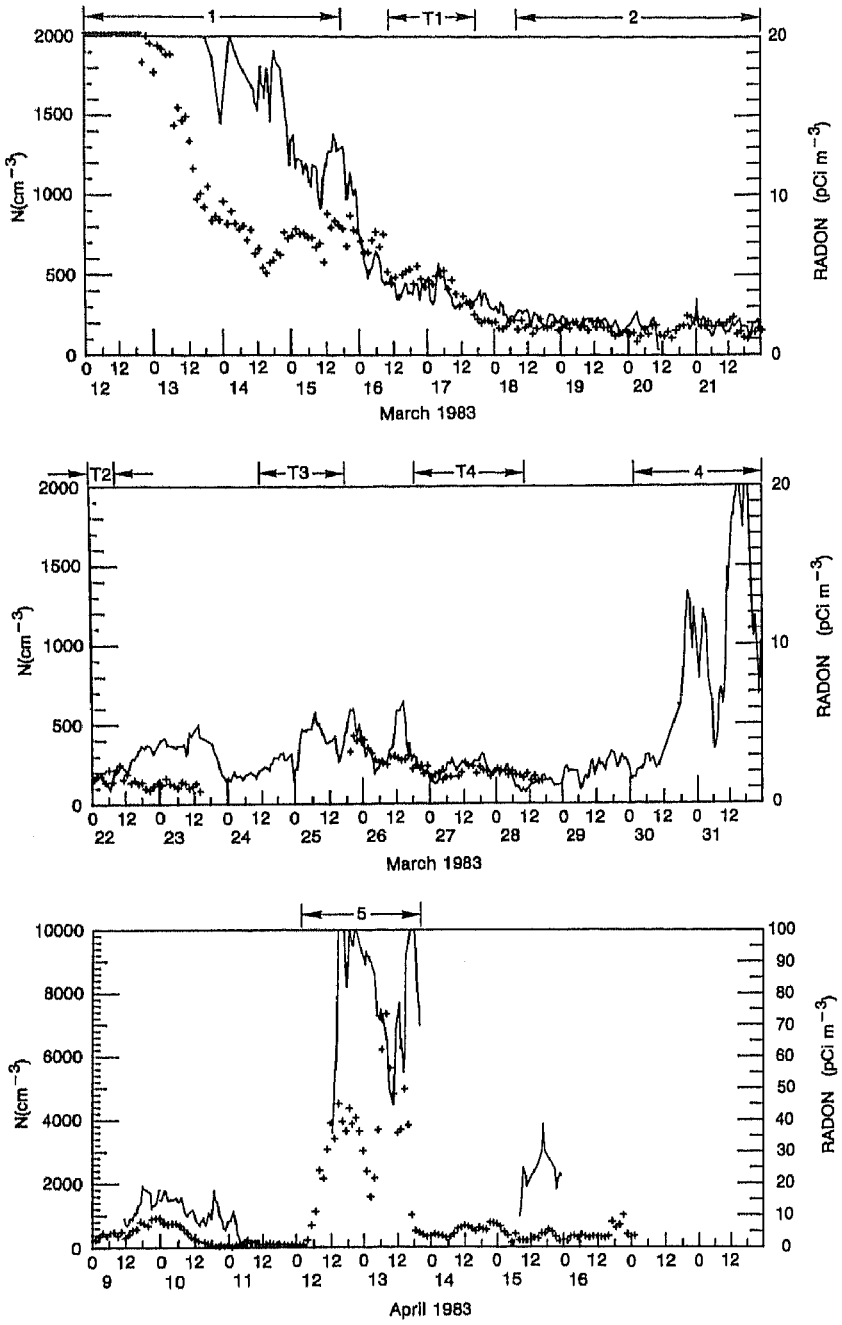

Fig. 6. Chronological history of total aerosol (solid curve) and radon concentrations (crosses) throughout the cruise. The numbered time periods refer to case studies discussed in section 3.

TABLE 1. Correlation Coefficients Between Wind Speed and Particle Concentrations

	Impactor				Mobility Analyzer		Aitkin Nuclei
	0.5–1, μm	1–2, μm	2–5, μm	5–9, μm	Large	Small	
Wind 0–12 hours	0.179	0.346	0.498	0.507	0.125	0.094	0.125
	0.630	0.659	0.782	0.644	0.172	0.137	0.095
Winds 0–24 hours	0.207	0.408	0.531	0.494	0.165	0.077	0.023
	0.674	0.736	0.809	0.666	0.092	0.126	−0.003
Mobility analyzer (large)	0.207	0.289	0.403	0.506	1.0		0.321
(0.173–0.53 μm)	0.346	0.386	0.445	0.066	1.0		0.839
Mobility analyzer (small)	−0.037	0.002	0.063	0.256		1.0	0.884
(0.022–0.173 μm)	0.241	0.232	0.312	0.093		1.0	0.929
Aitken nuclei	0.044	0.045	−0.065	0.066	0.321	0.884	1.0
	0.342	0.390	0.380	0.096	0.839	0.929	1.0

trations and the total aerosol concentration obtained by integrating the measured size distributions. Note that the aerosol concentration scale has been changed for the last leg of the cruise to accommodate the large concentrations encountered off the Iberian Coast. Since radon originates over land and decays with a 3.8-day half-life, it is a good indicator of the degree of continental influence remaining with the air mass. The scattering coefficients as measured with the MRI and HSS nephelometers are given in Figure 26 (section 5).

A vast amount of data (including approximately 1600 size distributions) were taken throughout the cruise. In the presentation of the aerosol size distributions which follows, we have chosen to limit the discussion to a number of episodes. The time periods of these episodes are shown along the top of Figure 6. The first episode shows the evolution of the size distribution from continental to marine during the 4 days following the ship's departure from Charleston, South Carolina, when the ship was in air advecting off the east coast of the United States. The decay in the aerosol and radon concentrations are clearly evident in Figure 6 as the air ages over the Atlantic. During the second period from March 18 to 21, the ship was in air which had a long history over the Atlantic, and the size distributions illustrate the characteristics of the background distributions measured over the remote tropical oceans. The episodes labeled T1–T4 are periods where changes in the size distributions were associated with known meteorological transitions. Episodes T1 and T3 are episodes where the passage of a meteorological disturbance brought air of African origin to the ship, whereas episodes T2 and T4 are times when precipitation scavenging is believed to have played an important role in removing particles. Episode 4 is the period of time when the ship approached the Canary Islands under optimum conditions for observing the aerosol plume downwind of the islands against the clean marine background. The last episode (episode 5) is the period when the ship traveled along the west coast of the Iberian Peninsula and encountered air advecting directly off the coast. During this period, new particle formation was observed on two occasions.

2.2. *Particle Concentration and Wind Speed Correlations*

Correlation coefficients between wind speed and the concentration of particles in various size ranges are shown in Table 1. The top value in Table 1 for each correlated pair was computed using all valid data obtained on the Charleston to Canary Islands leg of the cruise. The second value was computed after deleting data from the first 2 days of the cruise when the air at the ship was dominated by continental influence and during episodes of high concentrations of African dust. The second value should be more indicative of the correlation between sea-salt aerosol and wind speed. The instantaneous wind speed as well as the wind speed associated with the air parcel during the previous few days plays a major role in production of particles larger than 0.5 μm [*Gathman*, 1983] over the oceans. The wind histories used in Table 1 were determined from average speed between 12-hour segments of surface trajectory data and independently by estimating winds from weather maps. Similar wind histories were obtained by both methods.

The correlation of particles greater than 1 μm with wind speed was high for the subset of data which excluded periods when continental air was known to have been present. The much lower correlation found for the cruise as a whole must be a result of substantial continental material found in the large size range when the air mass could be traced to the continents. This is consistent with the chemical analysis of particles throughout the cruise [*Mack et al.*, 1986; *Parungo et al.*, 1984].

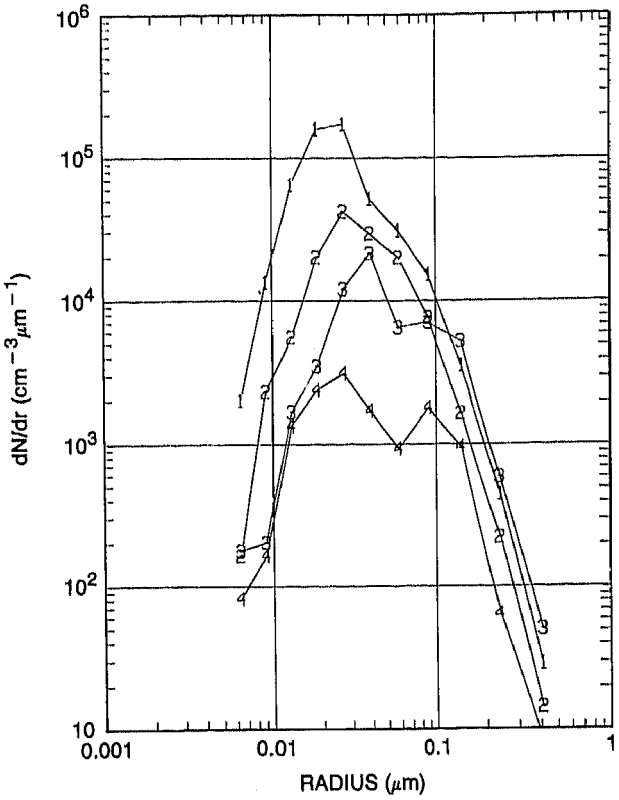

Fig. 7. Transition in the size distribution from continental to marine. The location at which the size distributions were taken are shown in Figure 9. Curve 4 is the size distribution for air with a long history over the Atlantic.

The concentrations of particles in the largest two channels of the mobility analyzer (0.173–0.53 μm) were combined, as were the concentrations in the next five smaller channels (0.022–0.173 μm), and correlated with wind and the total aerosol concentration (Aitken nuclei). Neither the Aitken nuclei nor mobility analyzer data were expected to correlate with wind, since most particles in this size range are of continental origin or produced in situ by gas-to-particle conversion. The excellent correlation between the mobility analyzer data and Aitken nuclei was expected since the Aitken nuclei are dominated by small particles measured with the mobility analyzer. Correlations between the wind speed and extinction are given in section 5.

3. SIZE DISTRIBUTIONS: CASE STUDIES

3.1. *Transition in Size Distribution From Continental to Marine*

The weather during the first 4 days was dominated by a strong low-pressure system moving out to sea off the middle Atlantic states. The night before sailing, there were heavy

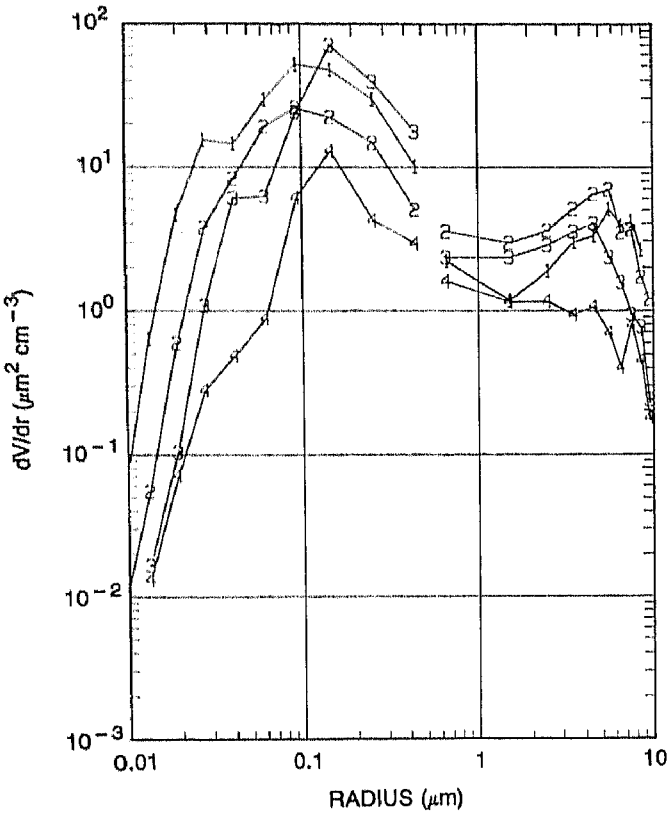

Fig. 8. Volume distributions during the transition from continental to marine corresponding to size distributions shown in Figure 7.

rains, and the skies were still overcast with high winds when the ship left Charleston and moved out into open seas at about 2100 UT (1600 EST) on March 11, 1983. The strong counterclockwise circulation around the center of the low resulted in northwest winds of 15 m s^{-1}. These were trailing winds, and it was necessary for the ship to turn periodically into the wind for about an hour to obtain air samples which were not contaminated by the ship's own exhaust. This transition is indicated as period 1 at the top of Figure 6.

Curve 1 of Figure 7 is the average of six size distributions taken between 2100 UT on March 11 and 2200 UT on March 12. The total aerosol concentration calculated from curve 1 is about 5460 cm^{-3}. During this period the skies were overcast with stratocumulus, and the radon count dropped from about 50 to 25 pCi m^{-3}, confirming that 1–5 hours earlier the air had been over land. Figure 8, curve 1 shows the corresponding volume distribution, and Figure 9 shows the back trajectory for this period of time. The volume distribution for particles with radii greater than 0.8 μm is that obtained from the Calspan impactor data. Because of the rapid change in the size distribution near the coast and the changing weather conditions, the six size distributions which were averaged to obtain curve 1 were all significantly different. This is in contrast to the rest of the "average" size distributions given in this report where we average only over periods where the size distribution remained nearly stationary over the averaging period. Curve 1 is given primarily to illustrate the larger features of the transition in the size distribution as the air leaves the continent.

Curve 2 is the average of 17 similar size distributions taken between 1100 and 2100 on March 14, giving a total particle concentration of 1920 cm^{-3}. The wind was from the west and had decreased to 3–5 m s^{-1}. It was no longer necessary for the ship to turn into the wind to obtain a valid sample, so sampling was performed continuously. Skies were nearly clear with about 10% cumulus cloud cover. The back trajectory for this period (Figure 9) shows that the air had been over the water for about 18 hours. The radon concentration had dropped to 7 pCi m^{-3}. Satellite photos (together with the air trajectories) indicate that the air came from a very clear area over Tennessee and behind the low-pressure system. Balloon soundings showed a strong inversion at about 4500 feet (1400 m) with a maximum relative humidity of only 90% at the inversion. The surface relative humidities were between 50 and 60% which are very low for the marine surface layer. From all indications the size distributions represented by curve 2 were taken in a subsident air mass originating over the United States and advecting to the location of the ship along a trajectory free of clouds.

Curve 3 of Figure 7 is the average of 14 similar size distributions taken on March 15 between 0930 and 1800 UT. The total concentration is 1325 cm^{-3}. The local wind speed was only about 3 m s^{-1}, and the direction was variable but from the southern quadrant. The skies during this period were overcast with 80–100% altocumulus and stratocumulus cloud coverage. The soundings showed a saturated region between 3800 and 5600 feet (1200 and 1700 m), capped by an inversion which was rising and broke up later in the day. (The following night there was rain.) Air trajectories (Figure 9) indicate that the air passed over the Georgia and northern Florida coast 2.5 days earlier. The satellite photos show very little cloud coverage along the trajectory until March 15, when significant cloud coverage was observed by local observations and balloon soundings. The radon concentrations remained at about the 7–8 pCi m^{-3} level during this period.

We believe that the hump at 0.1 μm which is evident in curve 3 is associated with the effect of nonprecipitating clouds on the size distribution. This hump did not occur during the time period represented by curve 2 where the air had traversed a cloud-free region between land and the measurement location. The possible effects of nonprecipitating clouds on the size distribution will be discussed later but will be alluded to throughout the presentation of the data as

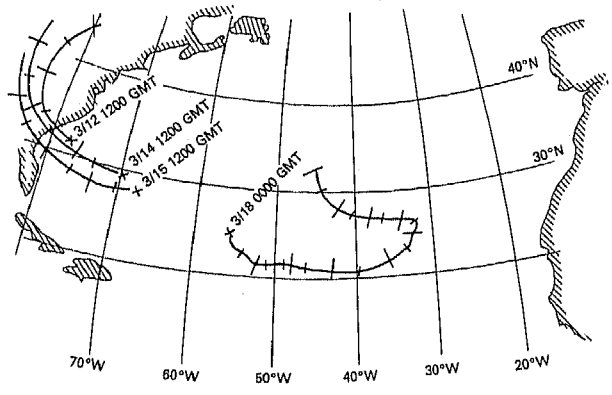

Fig. 9. Back trajectories for the four size distributions shown in Figures 7 and 8. Small (large) tic marks indicate 12 (24) hour intervals.

a possible cause for the frequently observed double-peaked distributions.

Figure 8, curve 3, shows the volume distribution during this time period. The very low winds (<3 m s^{-1}) during this period explain the low concentrations of particles greater than 5 μm. The impactor data which are used for the volume distribution at radii greater than 0.8 μm were taken less frequently than the DMA data. Curves 2 and 3 are the average of three individual distributions taken with the impactor during the specified time periods. The total volume in the DMA size range for curves 1–3 are 12.0, 6.0, and 14.5 $\times$ 10^{-6} cm^3 m^{-3}, respectively, while the corresponding impactor volumes are 27.5, 38.7, and 21.0 $\times$ 10^{-6} cm^3 m^{-3}.

3.2. *Typical Background Distributions Found in the Remote Atlantic*

During the night of March 15 and morning of March 16 a front passed over the ship bringing rain and heavy overcast which lasted most of March 16. After the passage of the disturbance the local winds were from the SE (trade winds) for several days with speeds generally below 7 m s^{-1}. Trajectory analysis showed (Figure 9) that the air had been over water for many days. The radon concentration dropped to 2 pCi m^{-3} which is normal for the Atlantic marine background level. Figure 10 shows the composite of 49 size distributions taken during the 35-hour period from 0800 UT on March 18 till 1900 UT on March 19. The composite is presented to emphasize that all the size distributions during this time period exhibited the double-peaked characteristic.

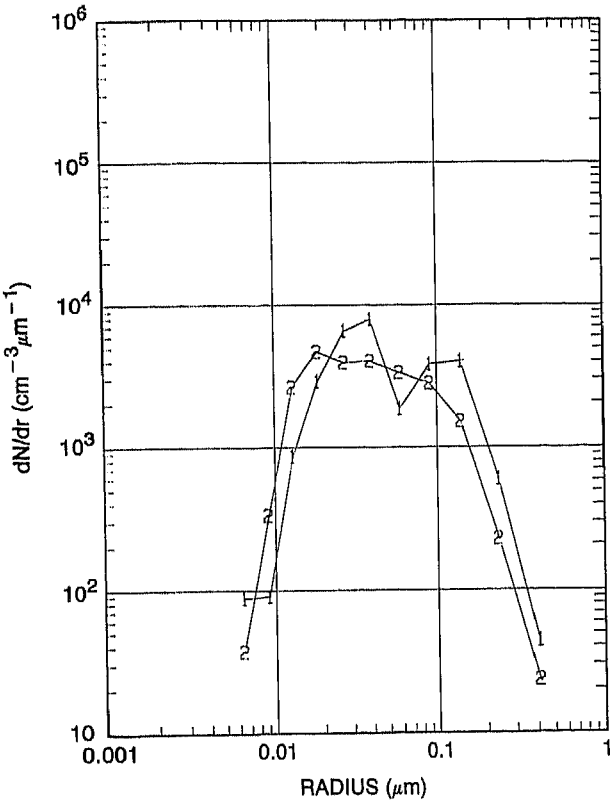

Fig. 11. Change in the size distribution during transit through weak front on March 16. Curves 1 and 2 are the average size distributions taken before and after passage of the front.

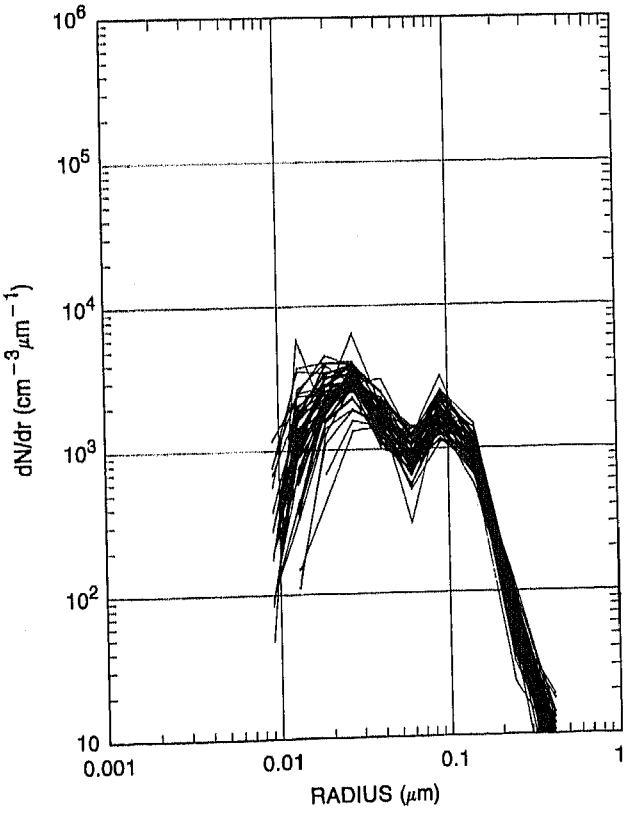

Fig. 10. Composite of 49 size distributions taken during a 35-hour period on March 18 and 19, typical of conditions when there was no continental influence.

The average total aerosol concentration is about 243 particles cm^{-3}. The soundings during this period indicate that the strong inversion which was present on March 13–15 had disappeared, and there were now multiple but weaker humidity inversions with higher humidities all the way up to 10,000 feet (3000 m). The cloud cover during this period varied. Throughout the day on March 18 there was about 85% coverage consisting of cirrus, cumulus, and altostratus, whereas on March 19 there was only about 20% cumulus coverage. Also, the double-peaked character of the size distributions appeared more pronounced on March 18 when the cloud cover was greater. The average of the composite is also shown as curve 4 on Figure 7 to compare the background marine size distribution with the series showing the transition from continental to marine.

During the period from March 18 to 21 the ship was under the influence of a subtropical high. The lower relative humidity in the marine boundary layer during this period would suggest that drier air from above was subsiding. The size distributions shown in Figure 10 are quite typical of the submicron size distributions measured during this 4-day period indicated as period 2 at the top of Figure 6.

There seems to be some mechanism in the remote (tropical) marine Atlantic which sustains the type size distribution shown in Figure 10. As will be pointed out later, there were occasions when the shape of the size distribution changed, but these changes were associated with synoptic scale meteorological disturbances. After the passage of the disturbance and the return of air with a marine history the

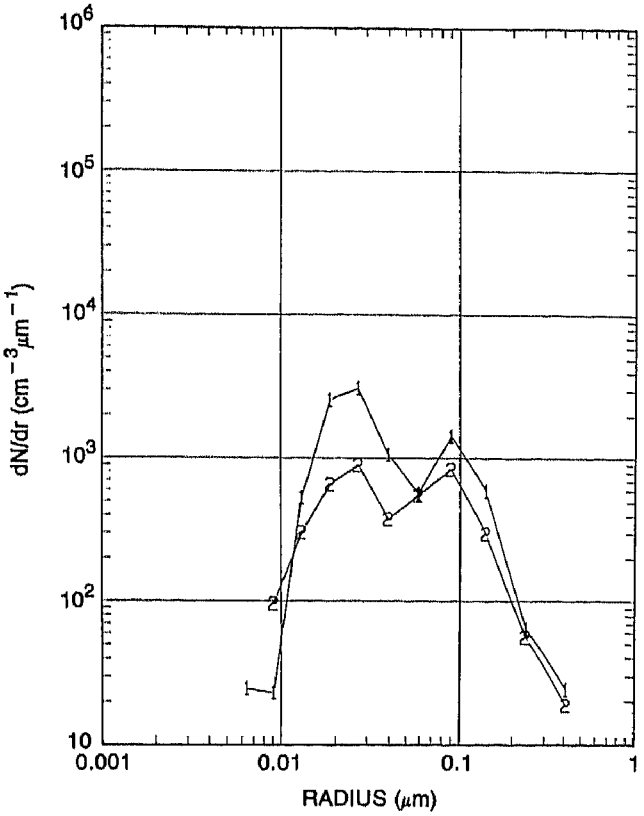

Fig. 12. Decrease in size distribution due to precipitation scavenging in local thunderstorms on March 22. Curves 1 and 2 are the size distributions taken before and after passing through a region of heavy local precipitation.

submicron size distribution seemed to always recover its double-peaked characteristic.

Figure 8, curve 4, shows the volume distribution where the distribution of the larger particles is the average of four impactor data sets taken during this period. The volume of particles with radius smaller than 0.6 μm is 2.27×10^{-6} cm^3 m^{-3} and the volume of particles larger than 0.7 μm is about 8.4×10^{-6} cm^3 m^{-3}.

3.3. *Periods of Meteorological Transitions*

On several occasions there were well-defined changes in the meteorological conditions often accompanied by some precipitation. Since aerosols are removed by precipitation scavenging, data taken before and after rain in the same air mass would be extremely valuable. The rain episodes were usually associated with meteorological disturbances, and it is difficult to determine whether the changes in the size distribution were associated with the rain or a change in the air mass. The change in the size distribution during four transitional periods are discussed here (episodes T1–T4 at the top of Figure 6).

3.3.1. *Case 1.* Late on March 15 the ship overtook a stagnating weak front. The skies were completely overcast from 1400 UT on March 15 until 0900 UT on March 17 with rain occurring much of the time from 0200 till 1300 UT on March 16. This event separated the two periods discussed above and marks the change from air which was influenced by North America to air of marine origin. The trajectories before and after this period (on March 15 and 18) are shown in Figure 9. On March 17 the midlevel air mass trajectory indicates that the air came from Africa about 8 days earlier.

Figure 11, curve 1, shows the average of six size distributions taken between 0020 and 0245 UT on March 16 before the ship encountered any rain but under overcast conditions, in air which most likely had some remnants of air from North America. Curve 2 shows the average of 14 size distributions taken between 1030 and 1945 UT on the same day, after the rain (there was some light rain during the early portion of the data). The soundings at 2300 UT on March 15 showed a saturated region from 2000 to 2700 feet (600 to 825 m) with neutral stability and moisture up to at least 10,000 feet (3000 m). The wind had shifted from west to southeast, and a large increase in relative humidity occurred late in the day on March 15. The radon concentrations remained at about 7 μCi m^{-3} on March 15 but dropped slowly on March 16 and 17, reaching values of about 2 μCi m^{-3} which is typical of pure marine air by March 18. The total number of particles represented by curves 1 and 2 are 747 and 464 cm^{-3}, respectively. Curve 2 shows no sign of the double-peaked characteristic. Size distributions similar to curve 2 but with somewhat less particles at radii less than 0.03 μm continued throughout the first half a day on March 17 before slowly transitioning to a double-peaked size distribution (shown by curve 4 of Figure 7) on March 18. The air encountered on March 17 could have originated over Africa, as suggested by *Parungo et al.* [1984], and/or had passed over the Lesser Antilles, as suggested by *Mack et al.* [1986]. Evidence for a

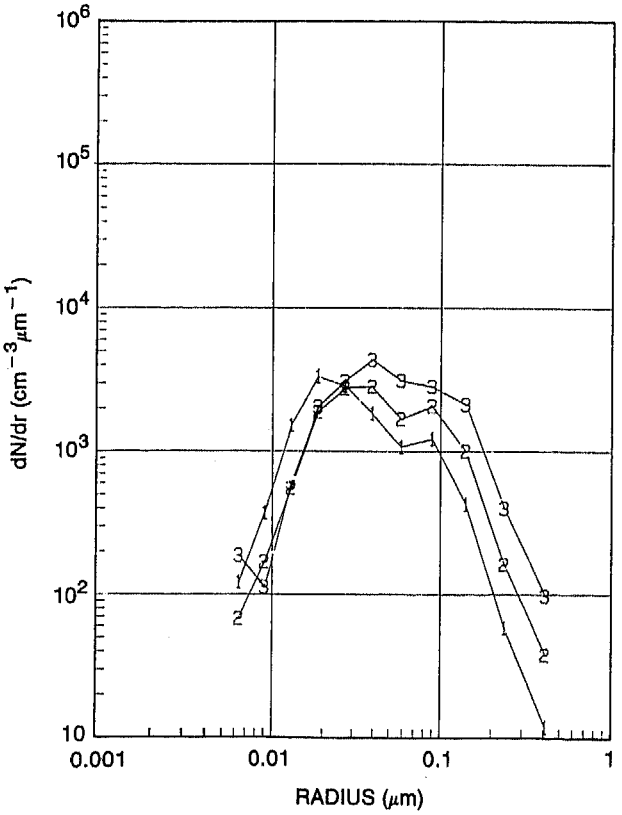

Fig. 13. Change in the size distribution as the ship encountered a weak trough containing air of African origin on March 24 and 25. Curve 1 was the distribution before entering the disturbed region, and curves 2 and 3 are the size distributions taken within the trough.

continental influence is based upon the air mass trajectory calculations and on the chemical analysis of the larger particles, which shows an abundance of silicon and other continentally derived components. We interpret the observed transition in the size distribution to be the result of the changing air mass.

3.3.2. *Case 2.* Early on March 22 the ship passed through a region of high thunderstorm activity (episode T2 in Figure 6). The local winds went from southerly at about 1 m s^{-1} to easterly at about 4 m s^{-1} at the beginning of this period. The cloud cover was about 60% cumulus (Cu) and cumulonimbus (Cb). The weather map showed scant evidence of a front, but a line of Cb was discernible on the satellite photo in the vicinity of the ship. The average of seven size distributions between 0015 and 0403 UT on March 22 is shown by curve 1 of Figure 12. During the night and early morning, there was frequent lightning in the area, and the ship's radar showed regions of heavy precipitation around and north of the ship. After some rain at the location of the ship at about 0530 UT, the size distribution shown by curve 2 (average of two) was observed. This type size distribution lasted for only about an hour. The total number of particles in the two size distributions are 186 and 96 cm^{-3}, respectively, and were some of the lowest aerosol concentrations measured during the cruise. We interpret the low concentration in the second size distribution to be the result of precipitation scavenging in local thunderstorms.

3.3.3. *Case 3.* During the period between 1200 UT on March 24 and 1200 UT on March 25, the ship passed through a region of a weak trough connected to a weak low north of the ship (episode T3 in Figure 6). Air trajectories at mid-levels and low levels indicate that the air was over Africa 7 days earlier. The Saharan origin of this air was reinforced by the detection of silicon and other elements associated with continental dust, found in particles of radius greater than 2 μm [*Parungo et al.*, 1984]. The radon counter was not functioning from midday on March 23 until late on March 25; however, the radon concentration at 2000 UT on March 25 was about 4 pCi m^{-3}, which was more than twice the concentration measured during the period of March 18–23 when the air was known to have a long trajectory over water. During the passage through the trough the wind direction changed from northerly to easterly, and the wind speed increased from a few meters per second to about 10 m s^{-1}. The cloud cover went from clear early on March 24 to about 50% Cu and Cb coverage with isolated thundershowers later in the day to completely overcast skies with some light rain showers on March 25. The skies remained overcast through March 26.

Figures 13 and 14 show the change in the size and volume distributions during this time. Curve 1 is the average of 13 mobility analyzer and one impactor size distributions taken during the period between 0220 and 1000 UT on March 24 just as the ship was entering the disturbed region. The winds were from the north with nearly clear skies early during the period with the appearance of Cb and distant rain late in the period. Curve 2 is the average of 13 mobility analyzer and one impactor size distributions taken between 1150 and 1930

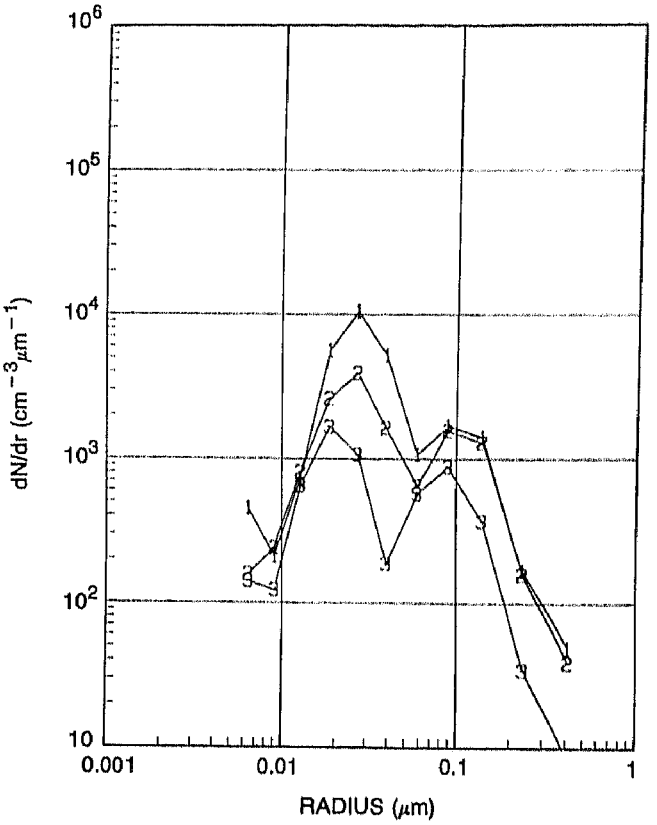

Fig. 15. Curves 1 and 2 are size distributions taken in air which had passed in front of a cold front and had encountered no (recent) precipitation, whereas the size distribution represented by curve 3 was taken in air which had passed through the cold front and encountered heavy precipitation 3 days prior to the measurement.

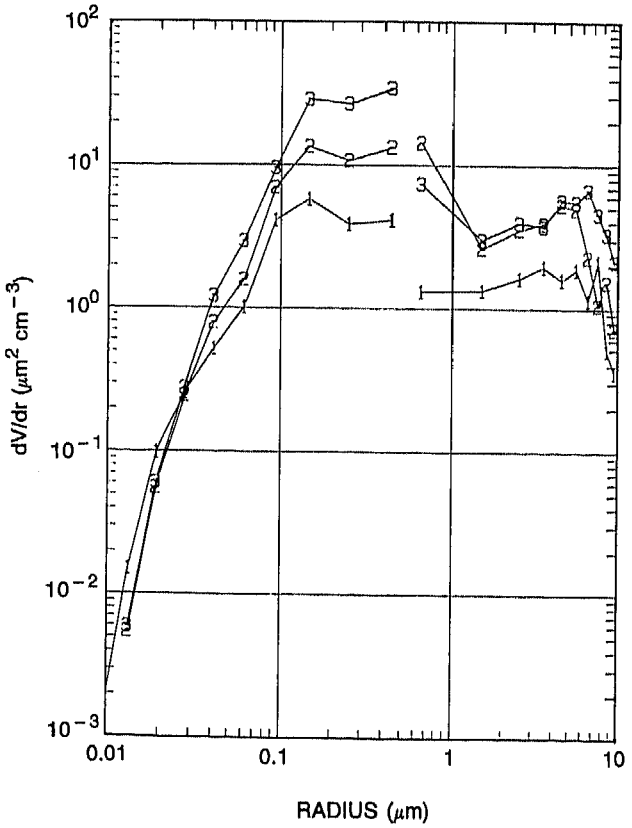

Fig. 14. Volume distributions corresponding to size distributions shown in Figure 13.

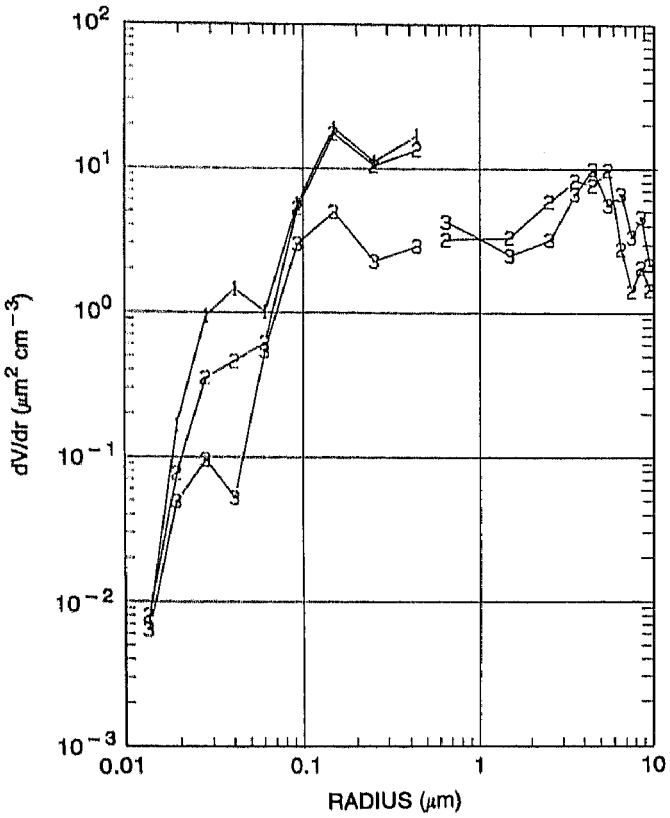

Fig. 16. Volume distributions corresponding to the size distributions shown in Figure 15.

UT on March 24. Again there were Cu and Cb with showers visible in the vicinity of the ship, and a definite change in the size distribution of submicron particles was observed.

Curve 3 is the average of 15 mobility analyzer and one impactor size distribution taken between 0530 and 1500 UT on March 25. The skies were overcast, and the wind had increased dramatically to about 10 m s^{-1} and was now from the east. There was some light rain at the ship's location just prior and just after this period, with some light drizzle during the early part of the period. Though there was a significant increase in wind speed, the seas had not yet responded, and there was no sea spray and only a few white caps. This, together with the continentally derived elements found in the analysis of larger particles, indicates that the increase in the concentration of larger particles was due to the change in the air mass and not to locally generated sea-salt particles. The total concentration of submicron particles in these three size distributions are 196, 299, and 506 cm^{-3}, respectively. The skies remained overcast and by 1700 UT the double-peaked characteristic returned and was fully restored by 1900 UT. The total concentration was higher (about 500 cm^{-3}), with a larger peak at 0.03 μm and also the number of large particles remained larger than observed in curve 4 of Figure 7. The size distribution on the following day (March 26) as the air mass trajectory shifted back over the North Atlantic is shown in Figure 15, curve 1.

The disappearance of the doubly peaked characteristic in both Figures 11 and 13 lasted for only a few hours and occurred in air which was believed to have been of Saharan origin. On both of these occasions there was extensive cloud cover; thus they were exceptions to the more common observation which associated the double peak with the presence of nonprecipitating clouds.

The volume distributions for this period are shown in Figure 14. The volume in the submicron size range (mobility analyzer data) for the three curves are 2.0, 5.5, and 13.2 × 10^{-6} cm^3 m^{-3}, respectively, and the volume for the impactor data is 13.9, 40.5, and 46.4 × 10^{-6} cm^3 m^{-3}. There was a large increase in the measured and calculated scattering coefficient during this period as discussed in section 5 and shown in Figure 26.

3.3.4. *Case 4.* Curve 1 of Figure 15 shows the average of 20 size distributions for the period 0500–1630 UT on March 26, well after the ship's passage through the area of the trough. The back trajectory indicates that the air came from the North Atlantic, passing near (but not over) the Iberian Peninsula four days prior to arriving at the ship and over (or near) the Canary Islands 2 days prior to arriving at the ship. Curve 2 is the average of 18 size distributions taken under similar conditions during the period from 1800 UT on March 26 to 1200 UT on March 27. After these 2 days (curves 1 and 2), there was a significant change in the submicron size distribution to that shown in curve 3, which is the average of 10 size distributions taken between 0850 and 1310 UT on March 28. All three size distributions

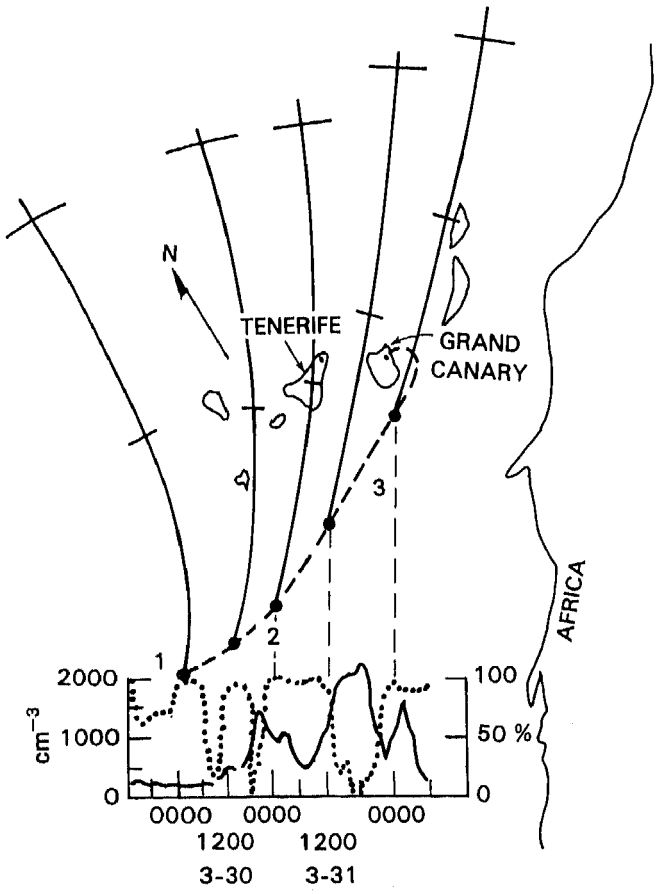

Fig. 17. Approach to the Canary Islands showing back trajectories of the air from the location of the ship. Tic marks indicate location of the air 12 and 24 hours prior to arrival at the ship. The dotted curve shows the percent of cloud cover at the ship, and the solid curve indicates total aerosol concentrations.

(curves 1–3) occurred under similar local meteorological conditions with mostly overcast skies of stratocumulus and altocumulus with air trajectories which originated in the North Atlantic. The wind speeds were 10–15 m s^{-1} from the northeast. The soundings for the three periods were similar and were characterized by a 1000-foot-thick (300-m) cloud layer capped by a strong inversion. The height of the inversion rose slowly during the 2-day period from about 3200 to 4500 feet (975 to 1375 m). The total concentrations of submicron particles dropped dramatically from about 438, to 273, and to 105 cm^{-3} for the three curves. There was a significant difference in the weather conditions along the back trajectory of the air for the three periods. On March 25 there was a strong cold front extending from a low over Europe, down across southern Spain, and out over the Atlantic, connecting to a high-pressure ridge in the Atlantic. The back trajectory for curve 3 was behind this cold front in a region of widespread precipitation 3 days prior to its arrival at the ship. The trajectories for the periods of curves 1 and 2 were always in front of the cold front, and the weather maps indicated that the air had not encountered a significant amount of precipitation for at least 5 days prior to reaching the ship. We therefore believe that the very low concentrations represented by curve 3 are associated with precipitation scavenging during passage through the cold front 3 days prior to arriving at the ship. If this interpretation is correct, then it follows that the size distribution had not recovered to the more typical submicron size distribution (such as curve 2) in the intervening 3 days.

Figure 16 shows the corresponding volume distributions. The integrated submicron volumes for the three DMA curves are 6.6, 5.6, and 1.4×10^{-6} cm^3 m^{-3}, respectively. There were no impactor data taken during the first time period and only one sample each during the second and third periods. The total impactor volumes for curves 2 and 3 are 46 and 49×10^{-6} cm^3 m^{-3}, respectively.

3.4. *Approach to the Canary Islands*

One of the most interesting periods of the 1983 cruise occurred when the ship approached the Canary islands from the southwest, as shown by the dashed line in Figure 17. Both radon measurements and back trajectories indicate that the air had been over the ocean for at least 9 days prior to passing over the Canary Islands. Because the air was free of any continental influence, the effect of the islands on the size distribution could be clearly seen. The back trajectory of the air arriving at the ship is shown in Figure 17, where the positions of the air 12 and 24 hours before are indicated by small and large tic marks on the trajectories. The aerosol plume downwind of Tenerife (population 400,000) and Grand Canary (population 600,000) are clearly visible, as evidenced by the peaks in the solid curve on the graph at the bottom of Figure 17. The dotted curve gives the cloud cover as observed at the location of the ship. Downwind of Tenerife, the marine inversion was capped with a heavy stratus deck, and complete cloud cover was reported at the Tenerife weather station 12 hours earlier. Figure 18 shows balloon soundings of temperature and relative humidity that indicate a stratus layer about 400 m thick with base near 900 m. Boundary layer modeling using the balloon sounding and measured sea surface temperature indicate that air from the surface would have mixed upward into the cloud deck in about 2 hours and would be mixed throughout the boundary layer in about six hours. The marine boundary layer (MBL) mixing is undoubtedly further enhanced because the islands are mountainous. We therefore can assume that the air from the island had been mixed throughout the cloud and bound-

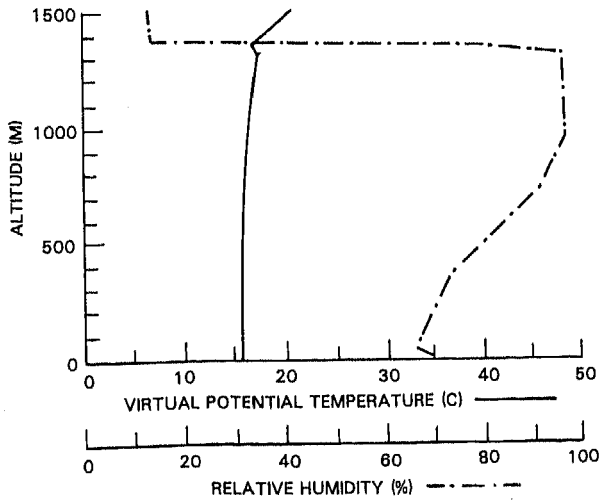

Fig. 18. Temperature and relative humidity sounding downwind of Tenerife.

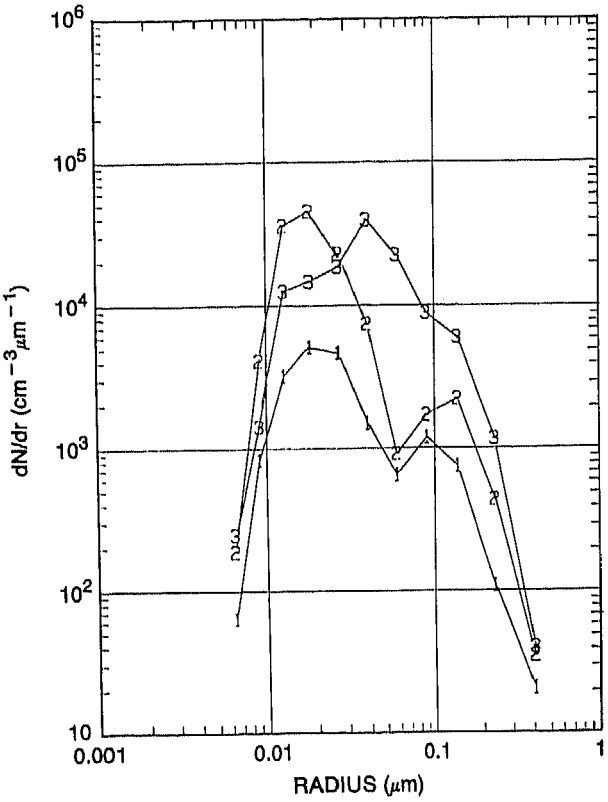

Fig. 19. Curve 1 is the size distribution before the ship was downwind of the islands. Curve 2 was taken downwind of Tenerife during heavy overcast conditions. Curve 3 was taken downwind of Grand Canary Island under clear conditions. The locations at which the three size distributions were taken are shown by the numbers along the ship's track in Figure 17.

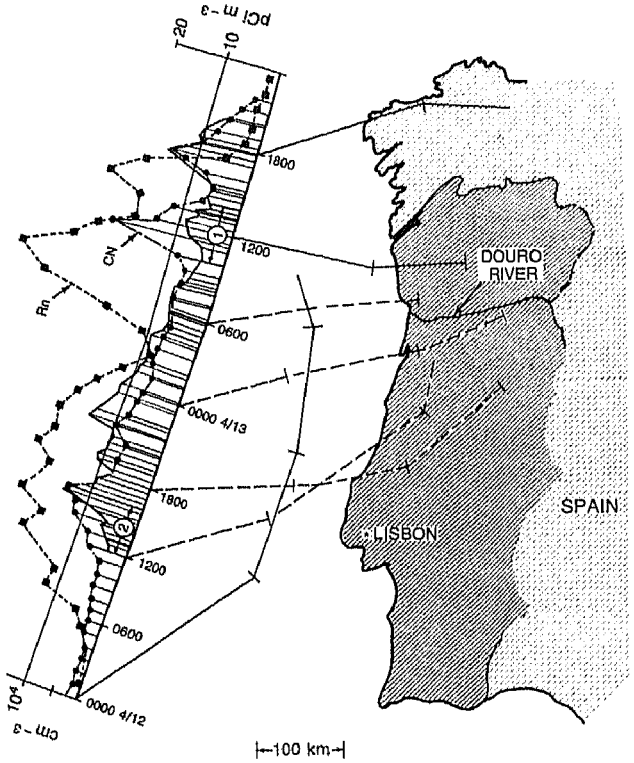

Fig. 20. Back trajectories for air encountered off the Iberian Peninsula where the tic marks indicate 6-hour intervals. Radon concentration (squares), CN concentrations (circles), and integrated aerosol concentrations (solid curve) measured along the track of the ship are plotted. (Scales are linear.) Time periods indicated by 1 and 2 refer to periods when the size distributions in Figures 22 and 23 were taken.

ary layer before arriving at the ship 12 hours later. Figure 17 shows that the increased aerosol concentration downwind of Tenerife had a local minimum between two small peaks at 0100 UT on March 31. This local minimum was associated with drizzle reported at the ship. About 18 hours later, when the ship was downwind of Grand Canary Island, the cloud cover had dissipated with the observed cloud cover at the ship dropping below 20% as shown by the dotted curve of Figure 17.

Figure 19 shows the size distributions observed during this period of time at the locations numbered along the ship's track. Curve 1 is the average of 19 distributions taken the night before the island influence was observed. Curve 2 is the average of 11 size distributions taken downwind of Tenerife between 1930 and 0345 UT on March 30, omitting a period when drizzle was reported at the ship (the air had traversed a heavy overcast region between the island and the ship). Curve 3 is the average of five distributions taken between 1500 and 1900 UT downwind of Grand Canary Island in air which had traversed nearly cloudless skies (less than 30% cloud cover). In addition to traversing nearly cloudless skies, there also was less time (4–8 hours) to cycle surface air through the few clouds which did exist. Downwind of Grand Canary the double-peaked feature had disappeared. Downwind of Tenerife where the air was more polluted than in the remote tropical Atlantic, the peak occurred at a larger radius (about 0.15 μm). If we assume that the peak at 0.1 μm is the residue of evaporated cloud droplets, then the larger size indicates a larger accumulation of material in the cloud droplet. The total number of particles in the three size distributions are 248, 1109, and 2336 cm^{-3}; the numbers of particles under the peak at about 0.1 μm for the first and second curves are about 105 and 260 cm^{-3}; and the total volumes are 3.3, 8.6, and 19.8 $\times$ 10^{-6} cm^3 m^{-3} for particles smaller than 0.6 μm. As the ship moved upwind of Grand Canary and just prior to arrival at Las Palmas (see Figure 17), the distribution was similar to that shown by curve 1.

3.5. *Air Advecting Off the Iberian Peninsula*

During the transit from the Canary Islands to Scotland the ship passed within 110 km of the Iberian coast. The ship's location as a function of time is shown in Figure 20. Circulation around a high-pressure system north of the ship and off the west coast of Ireland on April 11 produced winds from the northeast at 10 m s^{-1} causing high seas. Early on April 12 there was a squall with winds of about 16 m s^{-1}. On April 12 the high moved eastward, and the wind at the ship came increasingly from off the west coast of Portugal. The skies were mostly sunny but hazy, caused by high overcast of cirrostratus with some altostratus. As the winds switched more to the east, the fetch to the coast caused the winds and seas to decrease. Size distributions with the mobility analyzer were obtained from about 2000 UT on April 12 until about 2000 UT on April 13, at which time the ship again encountered heavy seas as it emerged from the (wind) shadow of the Spanish coast.

The NOAA trajectory analysis used earlier was not avail-

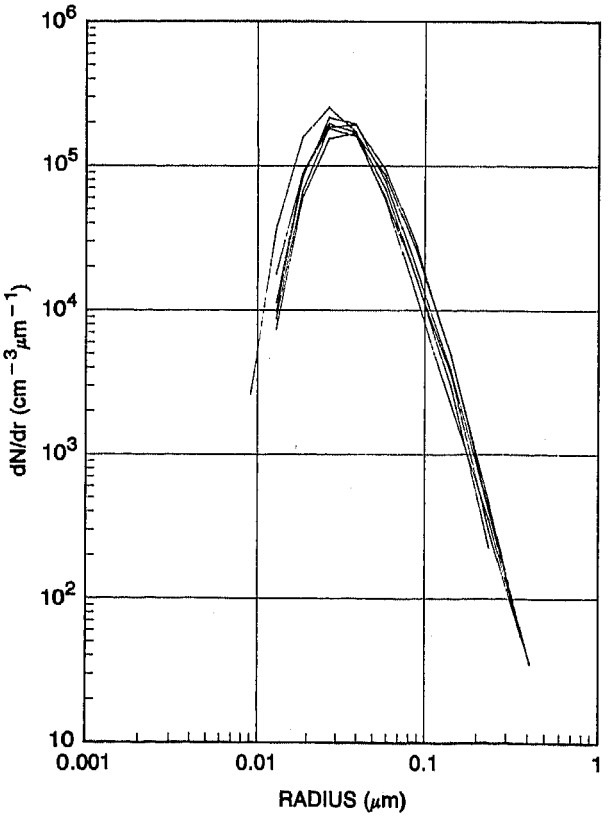

Fig. 21. Composite of six size distributions taken between 0400 and 0700 UT on April 13.

able on this leg of the cruise, so the back trajectories shown on Figure 20 were constructed from weather maps and local winds at the ship. The tic marks on the trajectories indicate 6-hour intervals. It is clear from the trajectories and radon data that there was an increasing influence of land during the morning of April 12. The radon increased dramatically from 2 to 20 pCi m^{-3} as the air came increasingly from the direction of land. Subsequent variations in the radon concentrations above 10 pCi m^{-3} are most likely due to variations in the source strength and mixing over land. The hourly condensation nuclei concentrations (circles) and the total aerosol concentrations from the submicron size distributions are also shown along the ship's track. The total concentrations are more than an order of magnitude greater than those found earlier in the remote Atlantic.

A composite of the six size distributions measured at the ship between 0400 and 0700 UT on April 13 is shown in Figure 21. This air had been over land about 12 hours earlier and had spent most of its 12-hour journey from the coast in darkness. These size distributions are very similar to those observed in air masses advecting off the east coast of the United States under similar conditions [*Hoppel et al.*, 1985]. The average total concentration of these six size distributions is 8000 cm^{-3}. The size distributions have a single peak and a rapid decrease of particles smaller than about 0.2 μm. The rapid decrease in concentration with decreasing size below 0.02 μm is predicted (by coagulation theory) to occur in the time the air has been over water provided there is no new particle formation. In addition to coagulation, the growth of very small particles caused by the condensation of

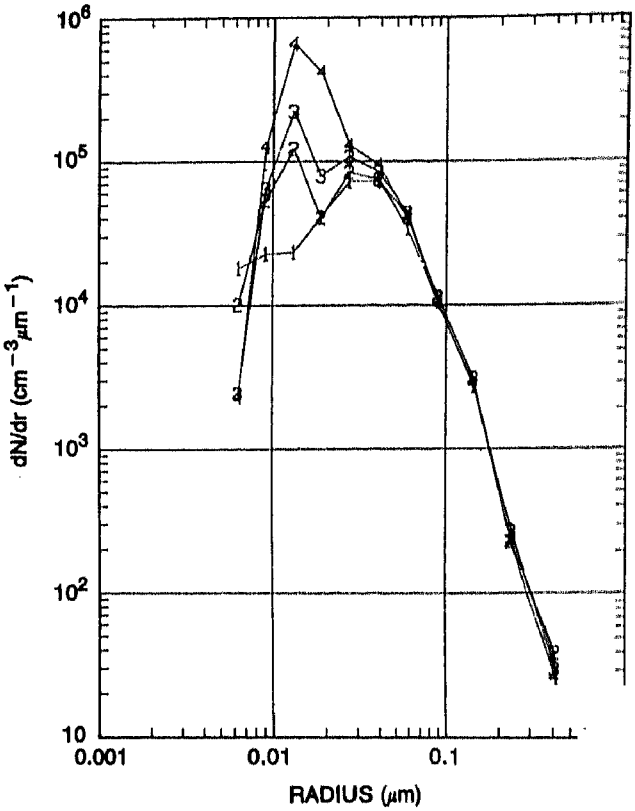

Fig. 23. Curves 1–4 show the evolution of the size distrib during period two (1150–1630 UT on March 12).

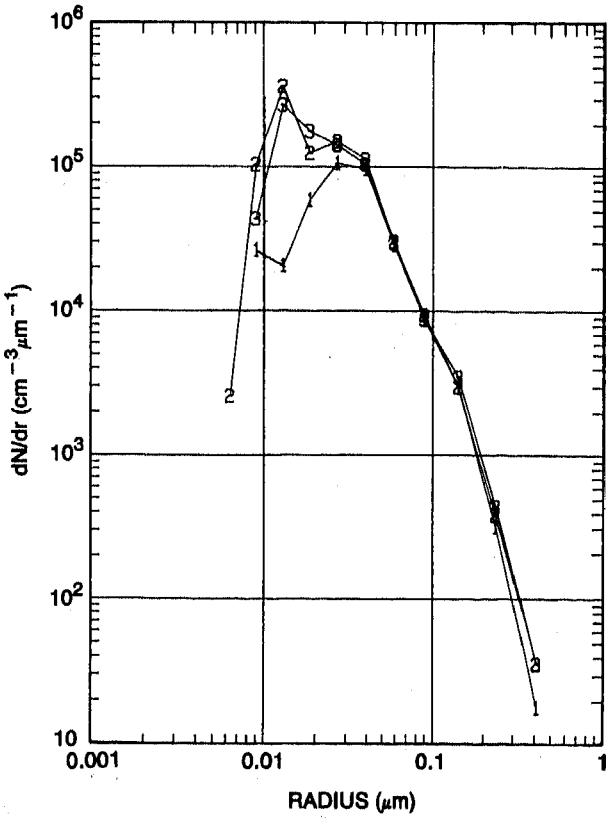

Fig. 22. Curves 1–3 show the evolution of the size distribution during period one (1020–1300 UT on April 13).

nonvolatile reaction products is an important mechanism moving particles from the very small sizes into the inter diate portion of the submicron size distribution.

There were two periods when an increase in very sm particles was observed. We believe these two periods we associated with homogeneous nucleation and growth of nc particles from gas phase reaction products. The times occurrence of these two periods are shown in Figure 20 the two circled numbers. Both occurred during midday in which had been over water throughout the morning. On bc occasions the concentrations of condensation nuclei m sured with the Gardner counter exceeded the total conc tration of particles measured with the mobility analyz indicating the existence of particles below the size ran detected by the mobility analyzer.

The size distributions between 1020 and 1300 UT on Apri 13 are shown in Figure 22. These size distributions followed those shown in Figure 21. Curve 1 is the average of two size distributions taken between 1020 and 1105 UT, curve 2 is the average of two distributions taken between 1110 and 1220 UT, and curve 3 is the average of two size distributions between 1225 and 1245 UT. The six size distributions were reduced to three for clarity of display. If the six are viewed individually, the same general evolution is apparent. The evolution of the distribution during the second event is shown in Figure 23. In this case we had no size distributions just prior to the event. Curve 1 is the average of two size distributions taken between 1155 and 1240 UT on March 12. Curve 2 is the average of two distributions taken between 1250 and 1330 UT, curve 3 is the average of two distributions

between 1340 and 1425 UT, and curve 4 is the average of four size distributions taken between 1430 and 1625 UT.

Since the two previous events occurred while the ship was close to land, a possible explanation might be that small particles encountered during these events were generated over land and advected to the location of the ship. However, this is unlikely because the air had been over water for 6–12 hours and coagulation calculations predict that particles in the 0.007–0.02 μm size range would be greatly reduced below their continental levels during the 6- to 12-hour period, and the resulting size distributions would resemble those shown in Figure 21. Another reasonable speculation might be that the small particles were due to ship traffic along the coast. But there was no visual sightings of ships upwind during these periods and it has been our experience that small particles from exhaust plumes of ships give more erratic and transient readings than those observed during these two events. The evolution of the distribution observed during these two events is similar to what is expected (based on calculations and chamber experiments of *Hoppel et al.* [1987]) for new particle formation and growth from gas phase reaction products. We therefore believe that during these periods we are observing spontaneous formation and growth of new particles directly from low-volatility products formed by gas phase reactions. Most likely, these reactions were photochemically induced since they occurred in air which had spent the morning daylight hours over water prior to arriving at the ship.

4. Discussion of Mechanisms Influencing the Submicron Aerosol Size Distribution

The size of an aerosol particle is a dynamic quantity which changes during its lifetime in response to a number of different processes acting on different time scales. In addition to the usual microscale aerosol mechanisms of coagulation and condensational growth, larger-scale atmospheric processes involving atmospheric transport and the passage of the aerosol through nonprecipitating and precipitating cloud cycles have profound effects on the size distribution. An important goal of this work is to determine the mechanisms responsible for producing the observed size distributions.

Since the lifetime of particles smaller than about 0.03 μm is estimated to be of the order of 1 day, the existence of particles in this size range indicates that there is a source of small particles over the remote oceanic regions. The accumulated evidence suggests that most of these particles, as well as particles as large as 0.2 μm, do not originate at the sea surface but are produced in situ from gas phase reaction products. The evidence against a surface source includes (1) the results of volatility measurements showing that particles smaller than several tenths of a micron are much more volatile than sea-salt particles, (2) the absence of any correlation between the concentrations of these particles and sea state or wind speed, (3) excess sulfate (above that contained in sea-salt aerosol) found in submicron particles in remote regions, and (4) an adequate supply of sulfur gases, which, under suitable conditions, have been shown to produce reaction products which are sufficiently involatile to form particulates. We believe the primary mechanisms responsible for the shape of the size distribution observed over the remote tropical oceans involve gas-to-particle conversion processes both inside and outside the clouds and scavenging of interstitial aerosol (particles too small to be cloud condensation nuclei (CCN)) by cloud droplets in nonprecipitating clouds. Because of the small concentrations of particles in remote regions, coagulation is not as important as it is in continental air masses.

4.1. *Gas-to-Particle Conversion*

Trace gases are continually being injected into the atmosphere from natural and anthropogenic sources. These volatile gases are removed from the atmosphere after they undergo chemical reactions which convert them to compounds which are less volatile. Chemical reactions can occur either in the gas phase (for example, photochemical reactions) or subsequent to absorption of the gas on existing particles or cloud droplets. In many cases, trace gases will pass through the particulate phase before removal by precipitation scavenging. There are three mechanisms for converting gases to particulate matter. Trace gases can be converted in the gas phase to less volatile products which (1) condense on particles causing growth of the existing population or (2) condense spontaneously to form new particles (homogeneous nucleation). (3) Trace gases can be absorbed into cloud droplets where they are converted to involatile compounds in the aqueous phase. The residue remaining after evaporation is an aerosol of increased mass.

Obviously, the relative importance of these three processes depends on the concentrations and chemical nature of the trace gases present in the atmosphere and on their reaction rates in either the gaseous or aqueous phase. It is well known that SO_2 emitted into the atmosphere by anthropogenic sources is a source of sulfuric acid and sulfate particles in continental air. Excess non–sea-salt sulfate found in remote oceanic aerosol particles has led to the conclusion that there must also be an oceanic source of sulfate. A primary source of this sulfate is thought to be dimethyl sulfide (DMS) (see, for example, *Bigg et al.* [1984]).

The yearly global injection of DMS from the oceans was estimated by *Andreae and Raemdonck* [1983] and *Andreae et al.* [1985] to be 40 ± 20 Tg S yr^{-1}, whereas *Bates et al.* [1987] estimate the global flux to be about 17 Tg S yr^{-1}. In either case, DMS is clearly a significant portion of the global natural sulfur flux of 60–90 Tg S yr^{-1} [*Andreae et al.*, 1985]. The natural and anthropogenic sources of sulfur are about equal, but most anthropogenic sulfur is emitted as SO_2 over the continents of the northern hemisphere. The importance of DMS as a source of sulfur in remote oceanic regions must be relatively large and could account for most of the non–sea-salt sulfate in marine aerosols. *Hatakeyama et al.* [1985] carried out experiments which indicated that the photooxidation of DMS gives about 21% SO_2 with the remaining sulfur being converted to methane sulfonic acid (MSA). Experiments by Hatakeyama et al. show that the photooxidation of DMS in humid air (relative humidity (R.H.) = 35%) containing 12 ppb DMS and 6 ppb NO produced large concentrations of particles in which both MSA and sulfuric acid were detected. Experiments by *Hoppel et al.* [1987] found that oxidation of DMS (~30 ppb) by simulated sunlight in a 600 m^{-3} chamber, which had previously been flushed with filtered outside air, initially produced a large number of very small particles ($r < 0.005$ μm). New particle formation ceased after about 10 min, and the existing parti-

cles grew throughout the subsequent 8 hours during which the air was irradiated. Growth ceased when the irradiation ceased. In these chamber experiments the concentration of DMS was much larger than that which exists in nature, and the extent to which they are representative of the natural environment is unknown.

The water-sulfuric acid system has been explored by a number of investigators [e.g., *Reiss*, 1950; *Mirabel and Katz*, 1974; *Hoppel*, 1975]. At 80% R.H., a sulfuric acid vapor pressure of only 10^{-16} atm is required to saturate the environment and 10^{-10} atm to supersaturate the environment sufficiently for homogeneous nucleation to occur [*Hoppel*, 1975]. At intermediate supersaturations, condensation will occur on existing particles. The MSA-water system has been investigated recently by *Hoppel* [1987] and shows that an MSA vapor pressure of less than 10^{-12} atm saturates the atmosphere at 80% R.H., while about 10^{-8} atm will cause homogeneous nucleation. It is clear that sulfuric acid has a greater nucleation potential than does MSA. Furthermore, it has been experimentally observed that the nucleation threshold for sulfuric acid is even less when ammonia is present (W. A. Hoppel, unpublished data, 1979). Presumably, the particles formed are ammonium sulfate. It is not our purpose here to champion any particular reaction but to illustrate that substances which have a high potential to nucleate new particles do exist in the marine environment. This is probably the source of the small particles observed over the oceans. Once formed, these particles will continue to grow by further condensation of reaction products. To make a quantitative estimate of particle growth, we will henceforth assume that disintegration of DMS is the only source of condensible material and that all the sulfur is converted to MSA or sulfuric acid. For growth estimates it makes little difference how the sulfur partitions between the two acids or if the acid is converted to sulfate, since all these products have about the same molecular weights.

If the flux of DMS is 140 μg S m^{-2} d^{-1} [*Bates et al.*, 1987] and if DMS is converted uniformly to a strong acid within a 1-km-thick marine boundary layer, then the volume production rate would be 0.14 μg S m^{-3} d^{-1}. If all the acid is converted to particulate matter, this would replenish 1.4 μg of S (4.2 μg of acid) m^{-3} in 10 days. Our data taken in the remote tropical regions indicate that the mass loading of particles smaller than 0.3 μm is typically in the 1–4 μg m^{-3} range. Thus the DMS injected into the atmosphere is sufficient, in itself, to sustain the observed aerosol load of small particles against removal, provided it is all converted to particulate matter.

4.1.1. *Condensational growth.* For condensational growth the radial growth law is given by

$$\frac{dr}{dt} = \frac{D'(r)}{\rho_p\, r}\,[\rho(\infty) - \rho(r)] \tag{1}$$

where r and ρ_p are the radius and density of the particle, $\rho(\infty)$ is the environmental vapor density of the condensing species, and $\rho(r)$ is the vapor density at the surface of the particle. (For a completely involatile species $\rho(r) = 0$.) $D'(r)$ is the effective diffusion coefficient given by

$$D'(r) = D\left[\frac{r}{r+\lambda} + \frac{4D}{rv}\right]^{-1}$$

where D is the diffusion coefficient for the condensing species, λ is its mean free path, and v is the mean thermal velocity. The effective diffusion coefficient accounts for the transition from the kinetic theory to the diffusion regime of condensation as the particle radius increases in size through the transition region ($r \simeq \lambda$). If the condensing species is being produced at a continuous rate by gas phase reactions in the atmosphere, then the environmental concentration is determined by a balance between the rate of mass production Q and the rate of diffusion to existing particles.

$$Q = 4\pi\rho(\infty) \int D'(r) r\, n(r)\, dr$$

or

$$\rho(\infty) = \frac{Q}{4\pi \int D'(r) r\, n(r)\, dr} \tag{2}$$

Since the conversion of sulfur also takes place within the cloud, the conversion rate within the cloud-free region will be less than the total conversion rate cited above (0.42 μg m^{-3} d^{-1}). For the purposes of the following estimates, we will assume that only half the sulfur is converted within the cloud-free air, and the other half will be reserved for conversion within the cloud. The growth for a newly formed particle of radius r growing through a background of absorbing aerosol particles of average size a and concentration Z is given by (from (1))

$$t = 4\pi\rho_p\left(\frac{aZ}{Q}\right)\frac{D'(a)}{D}\left[\tfrac{1}{2}(r-\lambda)^2 - \tfrac{1}{2}(r_c-\lambda)^2 + \lambda^2 \ln\left(\frac{r+\lambda}{r_c+\lambda}\right) + \frac{4D}{v}(r-r_c)\right] \tag{3}$$

where ρ_p is the density of the particle and r_c is the starting radius (assumed to be 0.005 μm in the following calculations). Taking the background particles to have an average radius of 0.08 μm and concentration (Z) of 300 cm^{-3}, the time to grow to 0.02 μm is about 1.4 days, whereas the times to grow to 0.04 and 0.08 μm are 3.4 and 7 days, respectively. Condensational growth would have considerable effect on the particle sizes below about 0.02 μm, whereas larger particles will experience little increase in their radius during their lifetimes.

4.1.2. *Nonprecipitating cloud cycles.* The source and persistence of the double-peaked size distributions observed in the remote tropical Atlantic as shown in Figure 10 was at first very puzzling. Coagulation and condensational growth would tend to fill in the gap. Our initial hypothesis was that the peak at 0.08 μm was caused by the generation of sea-salt particles at the sea surface and the peak at 0.03 μm was the result of small particles formed by gas-to-particle conversion. If this were the case, then the involatile sea-salt particles could be distinguished from the more volatile sulfates and nitrates by measuring the size distribution before and after passing the sample through a heated tube, as was done previously for CCN by *Twomey* [1968] and *Dinger et al.* [1970]. In a subsequent cruise (1984) aboard the NOAA ship *Discoverer* in the remote tropical Pacific, size distributions were taken alternately with and without passing the air

through a preheater. Similar double-peaked size distributions were observed without the heater but typically less than 5% of the particles under both peaks (smaller than 0.3 μm radius) were sufficiently involatile to be classed as sea-salt particles. A more likely explanation is that the minimum at about 0.05 μm and peak at about 0.1 μm are due to the action of cycling marine boundary layer air through nonprecipitating clouds which cap the marine boundary layer.

All cloud droplets are initially formed on a subset of aerosol particles which are called "cloud condensation nuclei" (CCN). During the cloud phase, the droplets absorb trace gases and convert some of the gaseous material to particulate matter. In addition to chemical conversion of trace gases, the smaller unactivated interstitial particles diffuse to the cloud droplets, transferring their mass to the much larger cloud droplets. When the cloud droplets later evaporate, the resulting residue is larger than the original cloud nucleus on which the droplet formed. Averaged globally, the nonprecipitating cloud cycles repeat themselves 10–25 times before a precipitating cloud system develops [*Pruppacher*, 1986]. Thus the aerosol is cycled through more than 10 nonprecipitating clouds (on the average) before the particles can be removed by precipitation scavenging.

Evidence supporting the nonprecipitating cloud hypothesis as the source of the double-peaked feature has been detailed by *Hoppel et al.* [1986] and includes (1) volatility measurements which show that the particles under both peaks are much too volatile to be sea-salt, (2) case studies which showed the double-peaked characteristic was associated with air which had passed through regions containing boundary layer clouds (see case studies given in sections 3.1 and 3.4), (3) the minimum between the two peaks occurs in the radius range 0.04–0.07 μm (from measured values of radius versus critical supersaturation [*Fitzgerald and Hoppel*, 1984], this would correspond to a critical supersaturation in the 0.1–0.4% range, in good agreement with expected cloud supersaturations), (4) the number of particles under the 0.09 μm peak is in the 50–130 cm^{-3} range, which is a reasonable number for cloud droplet concentrations in clouds, and (5) the source of convertible gases emanating from the sea surface is adequate to sustain the observed size distribution against removal mechanisms.

The rate at which particles grow out of a given size range during nonprecipitating cloud cycles can be estimated if the conversion rate of trace gases in the cloud phase is known. Cloud processes will only increase the mass of those particles which are large enough to act as CCN, and each cloud droplet will convert approximately the same amount of material regardless of the original size of the CCN. This means that the smaller CCN will show a larger fractional increase in mass than larger CCN. The growth rate of residual mass in a single cloud droplet M_p is related to the total mass conversion rate dM/dt by

$$\frac{dM_p}{dt} = \frac{1}{Z}\frac{dM}{dt}$$

where Z is the total number of cloud droplets. The equivalent dry radius growth rate (radius when water is removed) is

$$\frac{dr}{dt} = \frac{1}{4\pi\rho_p r^2 Z}\frac{dM}{dt}$$

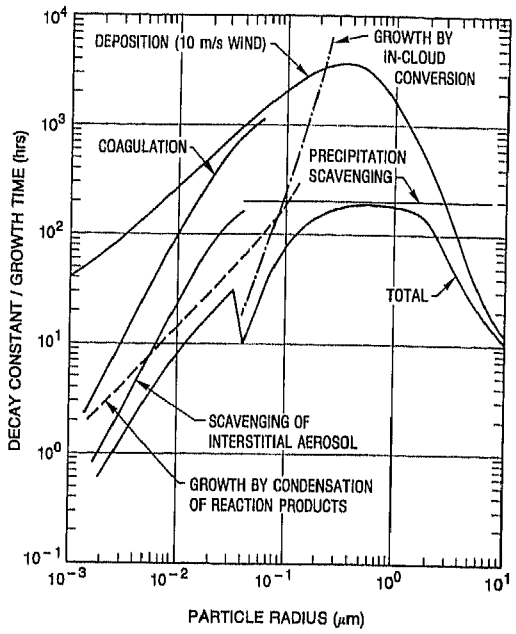

Fig. 24. Decay constants and/or growth times for various aerosol removal mechanisms. The heavy curve is the cumulative removal time.

where ρ_p is the density of the particle. Assuming a constant conversion rate, the time required for the radius of the dry aerosol (residue of cloud droplet) to increase its radius by 50% is given by

$$\tau_{50} = \frac{9.95\ \rho_p Z}{dM/dt}\, r^3 \qquad (4)$$

Assuming the in-cloud conversion rate to be 2.5×10^{-18} g cm^{-3} s^{-1} (one-half of the sulfur is converted in the cloud phase), then particles whose original radii are 0.04, 0.06, and 0.1 μm will increase their radius by 50% in 17, 58, and 270 hours, respectively. During their lifetime in the atmosphere (of the order of 10 days or less), particles larger than about 0.1 μm would experience very little growth, whereas smaller CCN would grow appreciably, causing a break in the size distribution at a radius determined by the cloud supersaturation. The accumulation of particles near 0.1 μm causes the steepening of the size distribution observed just above 0.1 μm (for example, see Figure 10). The exact location of the maximum which was usually observed to be near 0.09 μm will depend upon the in-cloud conversion rate and the concentration of cloud droplets Z.

4.2. *Loss of Interstitial Particles to Cloud Droplets*

Particles, too small to act as cloud condensation nuclei (interstitial particles), readily attach to the large surface area provided by the cloud droplets during the cloud cycles. The loss of particles too small for activation ($r < \sim 0.04$ μm) can be written as

$$\partial n(r)/\partial t = -n(r)\,K(r, a)Z$$

where Z is the concentration of cloud droplets and $K(r, a)$ is the attachment coefficient for a particle of radius r with cloud

droplets, all having radius a. The time constant for loss of interstitial particles to cloud droplets is

$$\tau_{\text{inter}} = 1/K(r, a)Z \quad (5)$$

The primary mechanisms for particle capture are Brownian diffusion and gravitational collection of interstitial particles by larger cloud droplets. For particles smaller than the critical radius (unactivated), attachment by diffusion is more important than gravitational collection and

$$K(r, a) = 4\pi D(r)a$$

where $D(r)$ is the diffusion coefficient of the particle. If the cloud droplets are assumed to have a radius of about 7 μm and a concentration of 200 cm^{-3} (liquid water content of 0.3 g m^{-3}) and if we further assume that the aerosol spends 5% of its time in a cloud (corresponding to 5% of the marine boundary layer occupied by clouds), then the calculated time constant for loss of interstitial particles to cloud droplets is 11 hours for 0.01 μm radius and 158 hours for 0.04 μm radius particles.

4.3. *Cumulative Removal Times*

In order to put the time scales discussed above into perspective, we have plotted the decay time constant and/or growth time in Figure 24 for each of mechanisms discussed above. For the cases of surface deposition, coagulation, and scavenging of interstitial particles the (exponential) decay time has a precise meaning. In the case of the surface deposition, the decay time is given by $H/v_d(r)$, where $v_d(r)$ is the deposition velocity for a particle of radius r and H is the height of the MBL. The deposition velocity used to obtain the deposition time plotted in Figure 24 is that given for a 10 m s^{-1} wind by *Giorgi* [1986, Figure 4]. For coagulation, the curve represents the decay time for a particle of radius r coagulating with particles of all other sizes as given by the size distribution shown in curve 4 of Figure 7 for the remote Atlantic. The decay time for interstitial particles is given by equation (5), and the numerical values used to evaluate the time constant were those given in section 4.2.

Also plotted are the growth times required for a particle of radius r to increase its radius by 50% either by condensation of gas phase reaction products or by in-cloud conversion processes, using the same assumptions as stated in the previous discussion. For the cloud case, only those particles large enough to be CCN will be affected. The growth time can be interpreted to be that time required for all the particles in a size interval between r and $(r + 1.5r)$ to grow out of that interval. Obviously, there is a danger of comparing growth times and (exponential) time constants. The growth time curves would be different had we assumed some other percentage growth. (Had we assumed a constant radial interval, instead of a fractional increase, even the slope of the curves would be different.) Nevertheless, we believe that Figure 24 is instructive in illustrating the relative time scales involved in the various processes.

The total time constant τ shown in Figure 24 was obtained from the following expression, where τ_i are the individual time constants and growth times:

$$\frac{1}{\tau_{\text{tot}}} = \sum_i \frac{1}{\tau_i}$$

Particles less than 0.01 μm are removed primarily by condensational growth and interstitial cloud scavenging with a time constant of 1–10 hours, and the mass is transferred to larger sizes. Particles with radii of the order of 0.02–0.03 μm have decay constants of the order of 1 day. Those particles which are large enough ($r > 0.04$ μm) to act as CCN during nonprecipitating cloud cycles gain additional mass during the cloud phase so that the smaller of the CCN grow rapidly, causing the minimum in τ_{tot}.

Precipitation scavenging is represented as a process which removes, with a time constant of 8 days, all particles large enough to be activated within the cloud. Precipitation scavenging (including all forms; nucleation scavenging, washout, and rainout) is the only important removal process in the size range of about 0.2–2 μm. For particles larger than about 5 μm, surface deposition is the important removal mechanism.

The larger population of particles found in the 0.02–0.2 μm radius range relative to the lower concentrations found at larger sizes, despite the shorter life of the smaller particles, indicates that mechanisms producing particles in the larger size range are much weaker than production in the 0.02–0.2 μm range. This is understandable since none of the mechanisms discussed can effectively transfer particles to sizes larger than about 0.2 μm on time scale short enough to be of importance in the MBL. Particles larger than about 0.5 μm are in most cases derived from the sea surface or advected from land. This interpretation is consistent with the observation that particles larger than 0.5 μm exhibit a much higher correlation with wind speed (Table 1) and sea state and are much less volatile than are particles smaller than 0.5 μm.

It is important to remember that Figure 24 assumes the size distribution observed in the remote tropical Atlantic. Use of a different size distribution, such as that observed off the west coast of the Iberian Peninsula, would result in a different cumulative curve than that shown. Most notably, the decay of small particles would be even more rapid, due to higher chemical conversion rates and increased rates of coagulation.

5. AEROSOL OPTICAL PROPERTIES

It is well known that absorption and scattering by aerosol particles in the atmosphere have an important effect on radiative transfer and the radiation budget of Earth. The aerosol optical thickness, being the vertically integrated value of attenuation due to aerosols, is thus an important climate parameter. The aerosol scattering coefficient, β_s, near the surface is of obvious importance due to its relationship to visibility expressed by the Koschmieder formula: $V = 3.91/\beta_s$. In addition, the aerosol optical properties of the lower atmosphere affect the performance of optical and infrared sensors used in numerous military systems.

This section presents the results of measurements of aerosol optical thickness and the near-surface aerosol scattering coefficient made on the 1983 Atlantic cruise.

5.1. *Aerosol Scattering Coefficient*

5.1.1. *Calculation of the scattering coefficient from the particle size distribution.* In addition to the measurements of the scattering coefficient, aerosol scattering and extinction coefficients were also calculated from the particle size distributions measured on the transatlantic leg of the cruise.

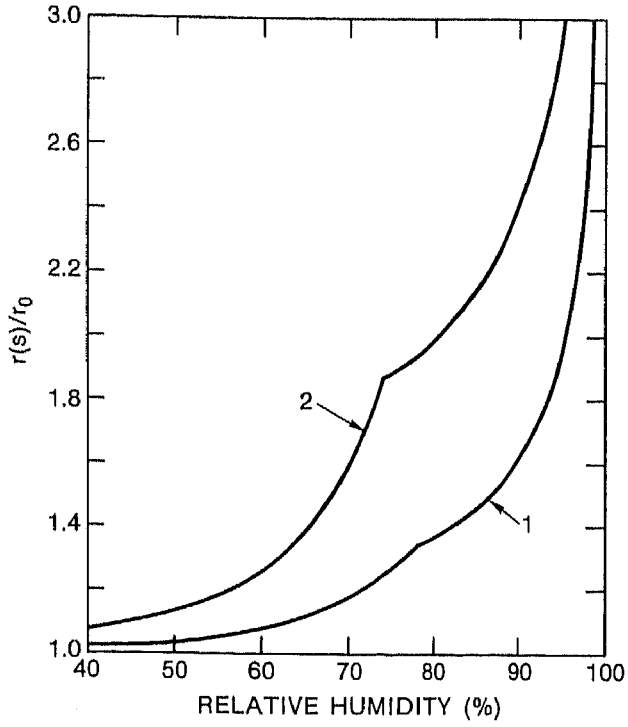

Fig. 25. Ratio r/r_0 of the radius of the wet to that of the dry particle as a function of relative humidity. Curve 1 is for particles with a radius <0.5 μm. Curve 2 is the growth curve for sea spray aerosols [*Hanel*, 1976] and applies to particles having a radius >1.5 μm. The growth curve of intermediate-sized particles (0.5 μm < $r \leq$ 1.5 μm) is obtained by interpolating between curves 1 and 2.

Scattering and extinction coefficients were calculated for 38 times between 1800 UT on March 13 and 1000 UT on March 31 when both impactor and mobility analyzer particle size measurements were available.

The scattering coefficient is defined in terms of the particle size distribution by

$$\beta_s = \int_0^\infty \pi r^2 Q_s(m, r, \lambda) n(r)\, dr \tag{6}$$

where Q_s is the Mie theory scattering efficiency factor and $n(r) = dN/dr$ is the differential particle size distribution. The definition of the extinction coefficient β_e is identical to (6) except that Q_e, the extinction efficiency factor, replaces Q_s. Q_s and Q_e are functions of particle index of refraction, m, and wavelength, λ.

The particle size distributions used to compute β_e and β_s were obtained by fitting a curve of the form

$$\ln [n(r)] = C_0 + C_1(\ln r) + C_2(\ln r)^2 + C_3(\ln r)^3 + \cdots$$

to the measured values of dN/dr between 0.05 and 8.5 μm. It was not necessary to fit the curve to data points below 0.05 μm since the smallest particles make a negligible contribution to the scattering and extinction at visible wavelengths. Since (6) cannot be integrated analytically, the particle size range was divided into 70 size intervals, and β_e was computed from

$$\beta_e = \sum_{i=1}^{70} \pi r_i^2 Q_e(m, r_i, \lambda) N_i \tag{7}$$

where r_i is the midpoint radius of each size interval and N_i is the number of particles in that interval. A Mie theory computer code developed by *Dave* [1968] was used to compute Q_s and Q_e.

The impactor samples particles outdoors, and it is assumed that it provides a particle size distribution at the ambient relative humidity. The mobility analyzer, on the other hand, measures the size distribution at a relative humidity less than ambient. The relative humidity in the mobility analyzer ranged from 11 to 27% below ambient. Thus, in order to calculate β_s and β_e for ambient relative humidity conditions it was necessary to adjust the size of particles smaller than 0.5 μm to account for the difference

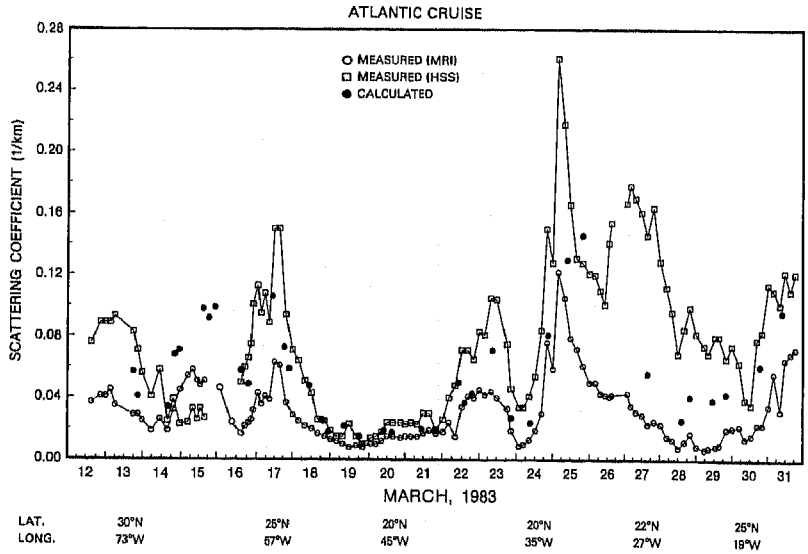

Fig. 26. Variations of the measured and calculated values of the aerosol scattering coefficient during the trans-Atlantic leg of the cruise.

between the mobility analyzer and ambient relative humidities. The adjustment was based on the model of equilibrium particle size as a function of relative humidity shown as curve 1 in Figure 25. The ordinate is the ratio of particle radius at the indicated humidity to particle radius in dry state. This particle growth model simulates the behavior of particles composed of 75% water-soluble material and 25% insoluble material. The soluble material is assumed to behave hygroscopically like mixtures of ammonium sulfate and ammonium nitrate, as described by *Hanel and Lehmann* [1981]. The effect of particle curvature on the growth curve is neglected, and curve 1 is applied to all particles, irrespective of their size in dry state. This simplification can be justified because the particle sizes for which the curvature effect is important contribute less than a few percent to the scattering and extinction coefficients at visible wavelengths.

The index of refraction of the particles must also be specified in order to calculate aerosol optical properties. The refractive index of particles at an ambient relative humidity S was computed from [*Hanel*, 1968]

$$n(S) = n_w + (n_0 - n_w)[r(S)/r_0]^{-3}$$
$$\kappa(S) = \kappa_w + (\kappa_0 - \kappa_w)[r(S)/r_0]^{-3} \quad (8)$$

where the swelling factor, $r(S)/r_0$, is the ratio of particle size at humidity S to its size in dry state, n and κ are the real and imaginary parts of the index of refraction, and the subscripts w and 0 refer to water and the dry particle, respectively. The swelling factor for particles smaller than 0.5 μm is given by curve 1 in Figure 25. Particles having a radius larger than 1.5 μm at the ambient relative humidity were assumed to be solution droplets formed on sea salt nuclei. For these particles, the swelling factor is given by curve 2 in Figure 25, which is the growth curve for sea spray aerosols [*Hanel*, 1976]. The observed hysteresis in the growth curve for sea-salt particles [*Hanel*, 1976] is taken into account, and below 74% relative humidity, curve 2 is the mean between the sea spray aerosol growth curves for increasing and decreasing relative humidity. For $r > 1.5$ μm, n_0 and κ_0 are the values for sea salt; for $r < 0.5$ μm, n_0 and κ_0 were computed as

$$n_0 = 0.75n_{ws} + 0.25n_d$$
$$\kappa_0 = 0.75\kappa_{ws} + 0.25\kappa_d \quad (9)$$

where the subscripts d and ws refer to insoluble and water-soluble materials, respectively. The index of refraction of water soluble material, insoluble material, sea salt, and water are taken from *Shettle and Fenn* [1979].

The swelling factor (growth curve) and index of refraction of particles in the range 0.5–1.5 μm were assumed to vary with particle size and were determined by interpolating between the values for the larger and smaller particles. Thus, on the average, the properties of the intermediate-sized particles were assumed to be more and more like those of sea salt as particle size approached 1.5 μm.

5.1.2. *Spatial variation.* Figure 26 shows the variation of the measured and calculated values of the aerosol scattering coefficient during the transatlantic leg of the cruise. HSS data are not included for the period from 2300 UT on March 15 to 1400 UT on March 16 because of the effects of precipitation and for the period from 1200 to 2300 UT on March 26 because the readings were affected by spray caused by the bow of the ship dipping into the waves. The MRI nephelometer was not operating from 1600 UT on March 15 to 0200 UT on March 16. For the sake of clarity we have plotted the data at 4-hour intervals. With the exception of the data for March 15 and for the period from about 1200 UT on March 26 to 1200 UT on March 29 it is seen that there is good tracking between the HSS and MRI values and between the measured and calculated values and that all three values agree to within a factor of about 2.

There are a number of factors which might have contributed to the large difference between the HSS and MRI values during the period March 26–29. First, the windows of the HSS instrument were not cleaned from 1200 UT on March 26 to 1500 UT on March 29. This was a period of high winds and rough seas and a significant coating of sea salt had accumulated on the windows of the HSS. When the instrument was recalibrated on March 29, it was found to be reading too low by about 50%. In order to salvage these data it was necessary to correct for the accumulation of deposit on the windows. This correction was made by using the observed wind speeds to estimate the rate at which the deposit built up over the 3-day period. However, in view of the large uncertainty in this estimate and the uncertainty of how the obscuring effect of the deposit varied with relative humidity, the accuracy of the corrected HSS readings is questionable.

A second factor which might have caused the corrected HSS to read too high during this period was the unusually weak wavelength dependence of the scattering coefficient. The primary calibration of the HSS, which uses a light source peaking at 0.88 μm, was obtained by plotting its output voltage against the scattering coefficient measured with an MRI integrating nephelometer operating at 0.475 μm. It is tacitly assumed by the manufacturer that this calibration is valid for all particle size distributions. However, since the variation of scattering coefficient with wavelength depends on the slope (shape) of the size distribution at the time of a given observation, it is possible that the HSS will overestimate or underestimate the scattering coefficient depending on whether the particle size distribution at the time of a given observation is much flatter or steeper than those used in obtaining the primary calibration. The ratio of the scattering coefficient at a wavelength of 0.475 μm to that at 0.88 μm was calculated from the curve fits to the mobility analyzer and impactor size distribution data. The value of this ratio for the period March 27–29 (no impactor data were obtained on March 26) ranged from 1.07 to 1.15. These were the lowest values of this ratio for the cruise. By contrast, the value of this ratio is about 1.8 for an aerosol having a Junge power law size distribution ($dN/dr \propto r^{-\nu}$) with $\nu = 4$ [*McCartney*, 1976]. This value of ν is typical of continental hazes. Further evidence that the accuracy of the HSS readings may depend on the particle size distribution is provided by the data for March 15. Figure 26 shows that this was the only period on the cruise when the HSS read lower than the MRI. During this period the ratio of the scattering coefficient at 0.475 μm to that at 0.88 μm was in the range of 2.2–2.3, the highest values calculated for the cruise. If the accuracy of the HSS depended on the slope of the size distribution one would expect a negative correlation between the ratio of HSS to MRI scattering coefficients and the ratio of the calculated scattering coefficient at 0.475 μm to

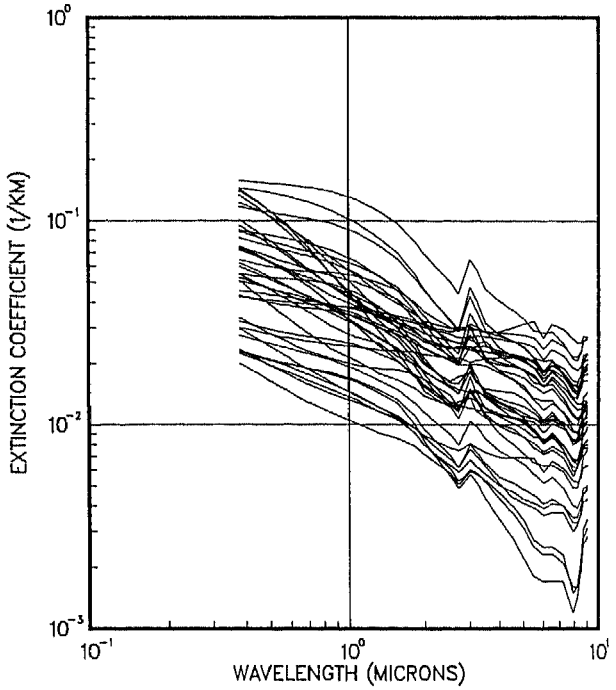

Fig. 27. Composite of the 38 curves of calculated aerosol extinction coefficient versus wavelength.

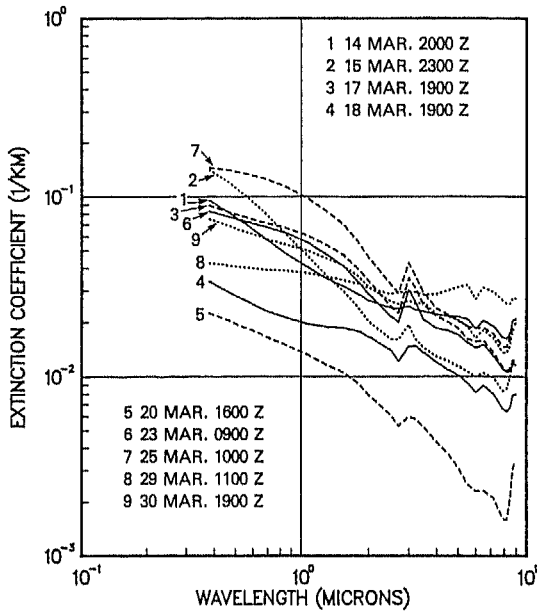

Fig. 28. Calculated aerosol extinction as a function of wavelength for nine selected times.

that at 0.88 μm. The correlation coefficient between these two ratios was computed to be -0.60.

The spatial variation of the scattering coefficient is due to variations in the size distribution and chemical composition of the aerosol particles. These variations in aerosol properties result from changes in meteorological conditions such as relative humidity, wind speed, and air mass history as well as from aerosol evolution due to processes such as coagulation and condensation. From March 13 to 14, the weather at the ship was influenced by the circulation around a departing low-pressure center. During this period there was a dramatic decrease in the west to northwest flow from the continent, an advection of drier air, increased subsidence and a decrease in particle concentrations as the air arriving at the ship lost its continental character. The decrease in aerosol scattering during this period reflects these changes. On March 15 the ship crossed the ridge line of the Bermuda high and entered the region of southeast trades. The period of the cruise within the subtropics, from about March 15 to 27, was not a continuous trade wind situation but was characterized by transient subtropical disturbances (troughs) which greatly influenced the weather along the ship's route. Upper level troughs affected conditions at the ship during March 16–18, 22, and 25–26. These disturbed periods were characterized by an increase in low and middle level cloudiness, an increase in wind speed and relative humidity (see Figure 2 and 4) and a less well defined boundary layer. Figure 26 shows that the aerosol scattering coefficient increased during these disturbed weather periods.

An analysis of air mass back trajectories computed for the period March 17–27 [*Parungo et al.*, 1984] shows that the air had transit times over water of at least 10 days prior to reaching the ship except on March 17, 23, and 25 during the periods of disturbed weather. The middle-level (850 mbar) trajectory for 1200 UT on March 23 showed that the air had originated over northern Africa 9 days earlier. On March 25, the 1200 UT trajectory indicates that both the low-level (1000 mbar) and middle-level air originated over Africa 4–8 days earlier. While the trajectories for March 17 do not trace the air back to Africa, they do show that the air had passed over the Lesser Antilles several days earlier. *Parungo et al.* [1984] measured the size distribution and chemical composition of particles collected on these 3 days, and they found increases in the concentration of particles larger than 0.5 μm radius and in the percentage of dustlike material (Si, Al, and Fe) contained in these particles. These aerosol measurements, together with the air trajectories, provide strong evidence for continental influence on these days. The high values of the scattering coefficient on March 17, 23, and 25 coincide with the times of suspected continental influence in the vicinity of the ship.

Values of the scattering coefficient of about 0.01 km^{-1} measured on March 19–20 are probably typical of the values for the remote subtropical North Atlantic under conditions of a well-defined boundary layer, clean maritime air (i.e., air which has resided over the oceans for at least 10 days) and low wind speeds.

5.1.3. *Wavelength dependence.* Figure 27 is a composite of the 38 curves of calculated aerosol extinction coefficient versus wavelength. It is seen that there is a wide range in the dependence of extinction on wavelength. Some of the curves exhibit a weak dependence on wavelength while others show a strong wavelength dependence over certain wavelength ranges. The variation of extinction with wavelength depends on the size distribution and chemical composition of the particles. Particle composition determines the wavelength dependence of the index of refraction. Relative humidity affects the amount of water on the particles and thus affects their refractive index, as described by equation (8). The increase in the value of the extinction coefficient at 3.0 and 8.7 μm wavelength is due to changes in the refractive index of the particles at these wavelengths.

TABLE 2. Percent Contribution to the Scattering Coefficient at 0.55 μm by Particles in Given Size Ranges

Date 1983	Time, UT	Particle Radius Range, μm			
		<0.15	0.15–0.5	0.5–1.0	>1.0
March 13	1800	10.3	49.9	8.2	31.6
	2100	10.8	54.0	10.4	24.8
March 14	1600	19.1	47.3	8.3	25.3
	2000	12.6	54.1	7.6	25.7
	2300	15.3	54.4	6.2	24.1
March 15	1500	14.0	74.0	4.7	7.3
	1900	11.8	70.6	5.8	11.8
	2300	11.0	70.8	7.7	10.5
March 16	1500	4.6	68.6	11.4	15.4
	1900	6.0	57.4	13.9	22.7
March 17	1100	2.2	44.3	30.0	23.5
	1900	2.8	45.2	25.3	26.7
	2200	4.3	48.1	18.5	29.1
March 18	1100	4.7	47.4	13.5	34.8
	1900	7.5	38.4	11.2	42.9
	2200	10.1	44.1	12.9	32.9
March 19	0900	8.9	55.1	12.9	23.1
	1800	11.2	47.8	13.7	27.3
March 20	1000	6.0	55.3	16.4	22.3
	1600	8.0	53.4	17.2	21.4
March 21	1100	6.7	44.7	23.9	24.7
	1900	6.0	52.5	24.6	16.9
March 22	1000	3.2	45.9	30.5	20.4
	1400	5.3	42.6	29.0	23.1
	1900	5.9	56.1	18.4	19.6
March 23	0900	2.7	46.9	27.5	22.9
	2100	6.4	37.7	21.8	34.1
March 24	0900	5.0	45.9	20.9	28.2
	2100	2.7	52.0	25.5	19.8
March 25	1000	2.5	57.8	22.6	17.1
	2000	2.3	44.4	28.4	24.9
March 27	1600	4.7	32.0	24.3	39.0
March 28	1400	4.3	24.1	8.6	63.0
	2000	2.8	33.4	12.3	51.5
March 29	1100	2.4	23.4	13.3	60.9
	2000	4.7	48.1	15.1	32.1
March 30	1900	6.6	45.0	18.5	29.9

Figure 28 shows the variation of extinction with wavelength for nine selected times. Each curve is representative of aerosol behavior over a period of at least 8 hours. Curve 2, for 2300 UT on March 15, shows the largest decrease in extinction over the wavelength range 0.5–2.0 μm. The size distribution at this time had the steepest slope in the range of 0.2–2.0 μm radius of any distribution measured on the cruise. Curve 5 exhibits the largest falloff in extinction above 2.0 μm wavelength. The size distribution (similar to curve 3 of Figure 13) from which this curve was calculated had the steepest slope above 1 μm radius observed on the Transatlantic portion of the cruise. The wind speeds for the 36 hours prior to 1600 UT on March 20 were less than about 2.0 m s^{-1}. Thus curve 5 is probably typical of the variation of extinction with wavelength in the infrared during extended periods of low wind speeds over the remote subtropical Atlantic. In contrast to curves 2 and 5, curve 8 displays a weak dependence of extinction on wavelength. The weak dependence of extinction on wavelength reflects the effect on the particle size distribution of a significant increase in the number of particles larger than 2 μm radius following four days of wind speeds in the range of 7–12 m s^{-1}.

Table 2 lists the percent contribution to the calculated scattering coefficient at 0.55 μm wavelength from particles in four size ranges. The relative contribution from different particle sizes depends on the particle size distribution. The contribution from particles smaller than 0.15 μm was largest during the early part of the cruise when the number of 0.1 μm particles was the highest, and the slope of the distribution in the submicron size range was the steepest. The contribution from particles between 0.15 and 0.5 μm ranged from 23 to 75%. The contribution from particles >1.0 μm radius ranged from 7 to 63%. The unusually large contribution that giant-sized particles made to the scattering at visible wavelengths on March 28 and 29 is due to the increase in the concentration of these particles, presumably as a result of high wind speeds.

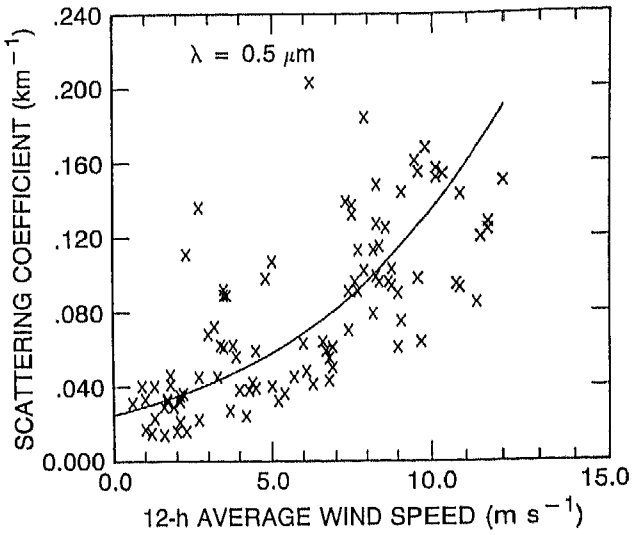

Fig. 29. HSS scattering coefficient as a function of 12-hour average wind speed. HSS values have been normalized to a relative humidity of 75%. The curve is a least squares exponential curve fit and is given by $\beta_s = 0.025 \exp(0.1689U)$, where U is wind speed in m s^{-1}.

5.1.4. *Wind speed dependence.* Figure 29 shows the HSS scattering coefficient as a function of 12-hour average wind speed. The HSS values plotted in Figure 29 have been normalized to a relative humidity of 75% in order to eliminate the effect of relative humidity changes on the variability of the scattering coefficient. The normalization was accomplished by computing the aerosol scattering coefficient as a function of relative humidity based on the particle growth model shown in Figure 25 and then multiplying the observed HSS value by the model-predicted ratio of the scattering coefficient at 75% R.H. to that at the ambient relative humidity. Values of the scattering coefficient at a wavelength of 5.0 μm, as calculated from the particle size distributions, are plotted as a function of wind speed in Figure 30. These values of the scattering coefficient have also been normalized to 75% relative humidity. It can be seen that there is considerable scatter in the data despite the removal of the effects of relative humidity variations. Much of this scatter can be attributed to variations in particle number densities due to variations in air mass history, atmospheric stability, and boundary layer depth. Variations in the amount of clouds in the boundary layer and hence variations in aerosol scavenging and modification by clouds may also contribute to the scatter. Despite the scatter in the data a dependence of

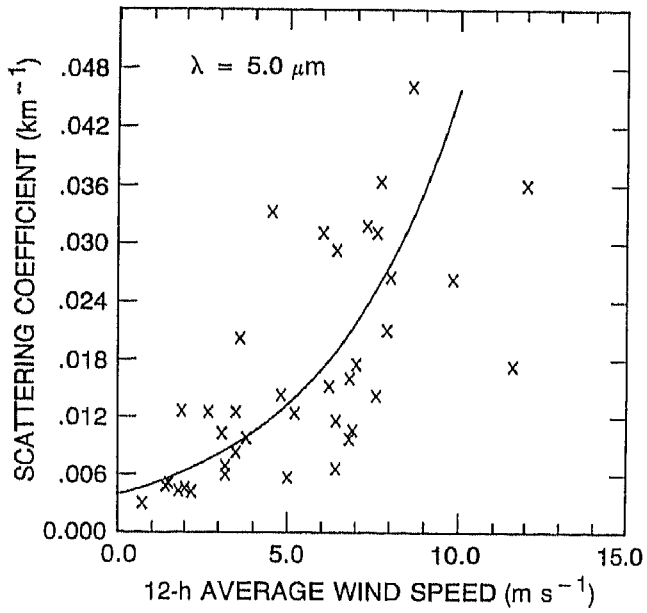

Fig. 30. Calculated scattering coefficient at a wavelength of 5.0 μm as a function of 12-hour average wind speed. The curve is a least squares exponential curve fit and is given by $\beta_s = 0.0039 \exp(0.2452U)$, where U is wind speed in m s^{-1}.

the scattering coefficient on wind speed is clearly evident. The curves in Figures 29 and 30 are least squares exponential curve fits to the data points and are an approximate description of the variation of the scattering coefficient with wind speed. The data also indicate that the scattering coefficient has a stronger dependence on wind speed at infrared wavelengths than at visible wavelengths. This suggests that the aerosol production mechanisms associated with the action of wind on the sea surface result in a greater percentage increase in the number of giant ($r > 1.0$ μm) particles than in the number of particles smaller than 0.5 μm. It is important to bear in mind that the curves in Figures 29 and 30 are approximations to the true variation of the scattering coefficient with wind speed that would be observed if all other meteorological conditions were the same over the range of wind speeds.

5.2. *Aerosol Optical Thickness*

5.2.1. *Method of measurement.* Aerosol optical thickness was determined from measurements of the total atmospheric optical thickness made with a Volz multiwavelength sun photometer. The total optical thickness $\tau(\lambda)$ is the vertical integral of the total attenuation coefficient due to aerosols, air molecules, and trace gases from the surface to the top of the atmosphere. The governing equation of the sun photometer is

$$I(\lambda) = I_0(\lambda) \exp[-\tau(\lambda)M] \quad (10)$$

where λ is wavelength, $I(\lambda)$ is the observed attenuated intensity of solar radiation in units of the sun photometer reading, $I_0(\lambda)$ is the instrument calibration which is the value of solar intensity the instrument would read at the top of the atmosphere, and M is the relative air mass at solar zenith angle ϕ. At the relatively small zenith angles at which measurements were made in this study, M is almost identically equal to the secant of ϕ. $\tau(\lambda)$ may be expressed as

$$\tau(\lambda) = \tau_a(\lambda) + \tau_R(\lambda)[P/1013] + \tau_0(\lambda) + \tau_g(\lambda) \quad (11)$$

where τ_R is the Rayleigh optical thickness at a sea level pressure of 1013 mbar, P is atmospheric pressure, τ_0 is the ozone optical thickness, and τ_g is the optical thickness due to absorption of solar irradiation by minor atmospheric gases, notably NO_2. Combining (10) and (11) gives

$$\tau_a(\lambda) = -(1/M) \ln[I(\lambda)/I_0(\lambda)] - \tau_R(\lambda)[P/1013] - \tau_0(\lambda) - \tau_g(\lambda) \quad (12)$$

The values of $\tau_R(\lambda)$ were taken to be the average of the values given by *Hoyt* [1977] and *Frohlich and Shaw* [1980] and are 4% lower than the earlier values of *Elterman* [1968]. (During the review of our manuscript, the paper by *Young* [1981] was brought to our attention. Young points out that *Hoyt*'s [1977] and *Frohlich and Shaw*'s [1980] attempts to revise the Rayleigh optical thickness values were incorrect and that correct use of depolarization data leads to τ_R values which are only 1.2% lower than those of *Elterman* [1968]. Use of the τ_R values suggested by *Young* [1981] would decrease the values of τ_a by only 0.007 at $\lambda = 0.44$ μm, by 0.004 at $\lambda = 0.5$ μm, and by 0.0015 at $\lambda = 0.64$ μm.) In the absence of independent observations of the vertical content of ozone we used the typical midlatitude value of $\tau_0 = 0.0092$ and 0.021 at $\lambda = 0.50$ and 0.64 μm, respectively. Ozone absorption can be neglected at 0.44 and 0.88 μm wavelengths. Further, since the measurements were made over remote ocean areas, we assumed that $\tau_g = 0$.

The sun photometer used on this cruise was a four-wavelength instrument with filters centered at 0.44, 0.50, 0.64, and 0.88 μm. The bandwidth at half-peak transmittance was less than 0.02 μm for all filters.

The sun photometer was calibrated by the Langley method using data collected during the cruise on days having clear skies or only small amounts of scattered cumulus

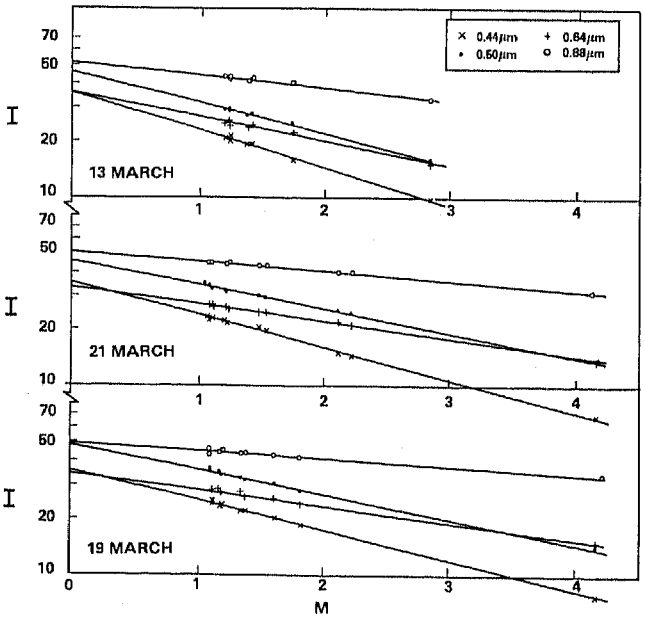

Fig. 31. Langley plots constructed from sun photometer measurements made on the Atlantic cruise. The abscissa is the relative air mass parameter.

clouds. In the Langley method a straight line is fitted to a plot of ln $[I(\lambda)]$ versus M for each wavelength. Extrapolation of these lines to $M = 0$ yields the calibration value $I_0(\lambda)$ for each wavelength. The calibration values used to compute aerosol optical thickness from (12) were obtained by averaging the $I_0(\lambda)$ values from three Langley plots. As discussed by *d'Almeida et al.* [1983], only those Langley plots should be accepted that have a strong linearity as expressed as a correlation coefficient between ln $[I(\lambda)]$ and M greater than 0.99. Figure 31 shows the Langley plots constructed from the sun photometer measurements made during the Atlantic cruise. These plots exhibit a correlation coefficient greater than 0.993.

The measured value of the aerosol optical thickness is the sum of tropospheric and stratospheric components. The normal background value of the stratospheric aerosol optical thickness is sufficiently small that little error is usually incurred in assuming that the tropospheric aerosol optical thickness is equal to the total measured aerosol optical thickness. However, since the measurements were made during a period (March 1983) when the stratospheric component was considerably enhanced above its background level due to the eruption of the El Chichon volcano in late March/early April 1982 and since our primary interest is in the tropospheric component of the optical thickness, it was necessary to estimate the El Chichon contribution and subtract it from the measured optical thickness. Sun photometer measurements of the spectral optical thickness of the El Chichon eruption cloud in the stratosphere were made on NASA aircraft flights in late April and early May 1983 [*Spinhirne and King*, 1985]. Based on these measurements, the stratospheric aerosol optical thickness at the time and latitudes of the cruise was estimated to be independent of wavelength in the visible part of the spectrum and to range from 0.08 at 30°N to 0.07 at 20°N.

5.2.2. *Spatial variation and wavelength dependence.* Figure 32 shows the spatial variation of the tropospheric component of the aerosol optical thickness at each of the sun photometer wavelengths. The values plotted for each day are the average of from three to nine hourly readings except for March 29 when only one reading (at 2200 UT) was

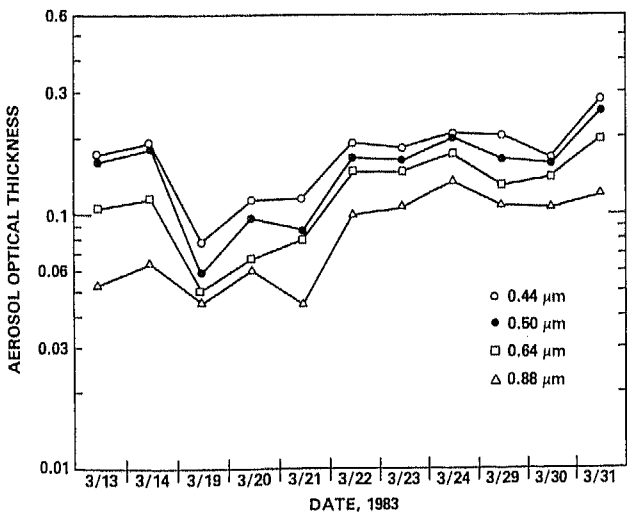

Fig. 32. Variation of the tropospheric component of the aerosol optical thickness along the ship's track.

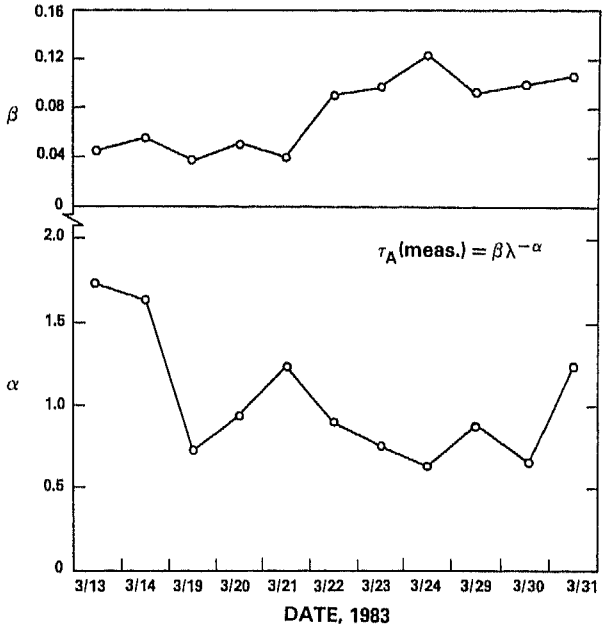

Fig. 33. Variations of the Angstrom parameters α and β along the ship's track.

obtained. Sun photometer measurements were made whenever possible. Cloud cover precluded measurements during the periods March 15–18 and March 25–28. The calibration values obtained from the Langley plots of the cruise data were used to compute the optical thicknesses. The lowest values of τ_a were measured between March 19 and 21. This was a period of low wind speeds and clean maritime air, as indicated by the air mass back trajectories which showed that the air had resided over the ocean for at least 9 days. The lowest values of the aerosol scattering coefficient were also recorded during this period.

The dependence of τ_a on wavelength in the visible and near-infrared spectral range can often be accurately described by the power law expression [*Angstrom*, 1964]

$$\tau_a(\lambda) = \beta\lambda^{-\alpha} \tag{13}$$

where wavelength is given in microns and β is the value of τ_a at $\lambda = 1$ μm. α and β are referred to as the Angstrom parameters. The exponent α is closely related to the slope of the particle size distribution at radii greater than 0.1 μm [*Bullrich*, 1964]. Since the wavelength dependence of τ_a is frequently described in the literature in terms of the Angstrom parameters, we calculated a least squares fit of (13) to the mean values of $\tau_a(\lambda)$ versus λ for each day for which there was data. The spatial variation of the Angstrom parameters is shown in Figure 33. The highest values of α occurred on March 13 and 14 when the air flow was off the east coast of the United States. The slope of the particle size distribution in the range 0.2–1.0 μm radius was steeper on March 13 and 14 than on any other day on which optical thickness measurements were made and is consistent with the high values of the Angstrom exponent.

The average values of α and β for the remote Atlantic (defined here as the portion of the cruise from March 19 to 29) are 0.84 and 0.08, respectively. *Tomasi and Prodi* [1982] measured aerosol optical thickness over equatorial areas of the Indian Ocean northeast of the Seychelles Islands in

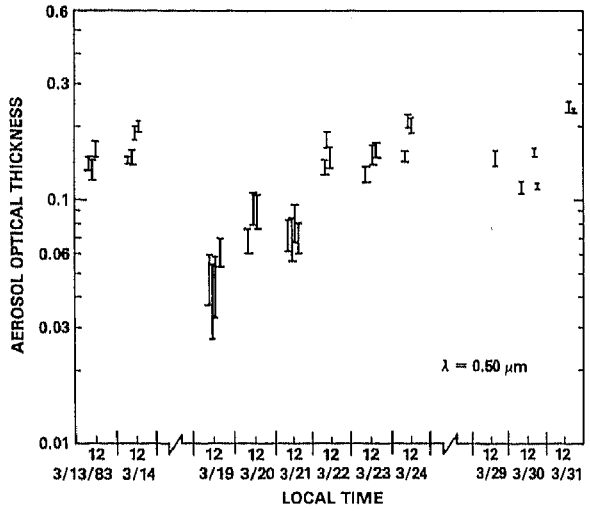

Fig. 34. Variation of the aerosol optical thickness, τ_a, at a wavelength of 0.5 μm. The vertical bars show the range in τ_a due to the uncertainty in the sun photometer calibration at this wavelength.

January and February of 1979, and they reported average values of α and β of 0.60 and 0.19. Thus, in the mean, the values of τ_a measured in the remote subtropical areas of the North Atlantic on this cruise are about half as large as those measured over the Indian Ocean by *Tomasi and Prodi* [1982].

Our primary interest is in the value of τ_a at a wavelength of 0.5 μm. Figure 34 shows the spatial variation of τ_a at λ = 0.5 μm in greater detail than Figure 32. Although readings were taken hourly on a number of days, values are plotted at intervals of 2 hours for clarity. A range of values of τ_a is plotted for each time. The high values were computed using the sun photometer calibration values obtained from the Langley plots of the cruise data. The low values were computed using calibration values determined by the manufacturer, who recalibrated the instrument several months after the cruise. Thus, we feel confident that the correct values of τ_a at λ = 0.5 μm lie within the range shown.

5.2.3. *Comparison of measured and calculated optical thickness.* It is generally believed that the marine boundary layer makes the major contribution to the tropospheric aerosol optical thickness over remote regions of the Atlantic, except during episodes of Saharan dust transport. It is instructive, therefore, to compare the measured tropospheric aerosol optical thickness with the calculated aerosol optical thickness of the boundary layer. It is of particular interest to determine if the observed variation in the measured optical thickness can be explained by variations in the height and relative humidity of the boundary layer together with variations in the aerosol scattering (or extinction) coefficient at the surface.

The aerosol optical thickness of the boundary layer is defined by

$$\tau_{a,B} = \int_{z_0}^{H} \beta_e(z)\, dz \qquad (14)$$

where H is the height of the boundary layer and z_0 ($\simeq$10 m) is the height of the shipboard observations. For the purpose of the calculations we express $\tau_{a,B}$ as

$$\tau_{a,B} = \beta_e(z_0) \int_{z_0}^{H} \left[\frac{\beta_e(z)}{\beta_e(z_0)}\right] dz \qquad (15)$$

where $\beta_e(z_0)$ is the value of β_e at $z = z_0$. Thus $\tau_{a,B}$ is the product of the extinction coefficient at the surface and the integral of the normalized extinction coefficient, $\beta_e(z)/\beta_e(z_0)$, over the depth of the boundary layer.

Because of the variable weather conditions during the Atlantic crossing, the boundary layer varied from being well defined, with the relative humidity decreasing sharply from its peak value to below 30% over a distance of 15–30 m at the base of the overlying inversion, to being less well defined with the relative humidity decreasing from its peak value to 50% over a distance of 600 m in one case. For the purpose of these calculations we define the top of the boundary layer to be the height at which the relative humidity decreases to its value at the surface after reaching its peak value.

The vertical profiles of $\beta_e(z)/\beta_e(z_0)$ needed to calculate $\tau_{a,B}$ were determined by combining the profiles of relative humidity from the soundings and a simple model of the vertical variation of particle concentrations with the calculated values of aerosol extinction as a function of relative humidity. Aerosol extinction as a function of relative humidity was calculated from the measured aerosol size distribution and the model of particle size and refractive index as a function of relative humidity described earlier. The atmosphere was assumed to be well mixed from shipboard level up to the height of maximum relative humidity, and total particle concentrations were assumed to be constant with height; that is, the aerosol size distribution normalized to the

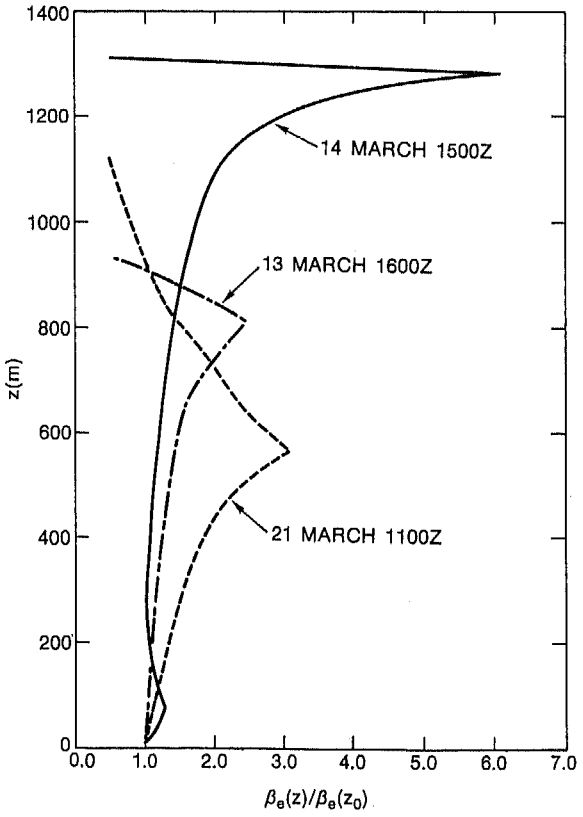

Fig. 35. The computed profile of the normalized extinction coefficient, $\beta_e(z)/\beta_e(z_0)$, for three selected times.

TABLE 3. Values of H, ζ, and $\beta_s(z_0)$ at the Times for Which the Boundary Layer Optical Thickness Was Computed

Date 1983	Time of Sounding, UT	Time of τ_a (meas), UT	τ_a (meas)	H, km	ζ, km	$\beta_s(z_0)$, km^{-1}	
						β_s (MRI)	β_s (HSS)
March 13	1528	1600	0.133	0.95	1.32	0.030	0.085
March 14	1455	1500	0.150	1.32	2.09	0.018	0.024
	1948	2005	0.197	1.50	2.70	0.032	0.042
March 19	1512	1500	0.041	0.65	0.88	0.012	0.021
	1833	1800	0.050	0.70	0.92	0.008	0.014
March 20	1254	1400	0.091	1.30	1.95	0.014	0.026
	1617	1600	0.090	1.10	1.85	0.015	0.025
March 21	0943	1100	0.066	1.05	1.75	0.015	0.027
	1548	1600	0.080	1.35	1.68	0.019	0.029
March 22	0948	1100	0.157	0.95	1.44	0.030	0.062
March 23	1459	1500	0.153	0.65	0.89	0.038	0.086
	1802	1700	0.160	0.70	0.99	0.034	0.070
March 24	1454	1417	0.201	1.25	1.74	0.020	0.055
March 30	0930[a]	0930	0.133	1.60	2.17	0.012	0.030
	1720[b]	1720	0.157	1.25	1.97	0.022	0.071
March 31	1455[c]	1455	0.240	0.90	1.32	0.071	0.118

[a]Humidity profile for 0930 UT estimated from soundings at 0700 and 1024 UT.
[b]Humidity profile for 1720 UT estimated from soundings at 1437 and 2003 UT.
[c]Humidity profile for 1455 UT estimated from sounding at 0845 UT and from observed change from overcast to mostly clear skies.

surface relative humidity was assumed to be independent of height in this portion of the boundary layer. As noted by *Fairall and Davidson* [1986], small particles are expected to observe mixed layer scaling which is usually taken to mean the absence of a vertical gradient. However, between the height of maximum relative humidity and the top of the boundary layer, particle concentrations were arbitrarily assumed to decrease linearly with height to 50% of the surface concentrations. Figure 35 shows several of the computed profiles of the normalized extinction coefficient. The integral in equation (15), which we denote by ζ, was evaluated from the profiles of $\beta_e(z)/\beta_e(z_0)$. Thus $\tau_{a,B} = \beta_e(z_0)\zeta$. The values of $\beta_e(z_0)$ at $\lambda = 0.50$ μm were obtained by multiplying the measured values of $\beta_s(z_0)$ at wavelength of λ_1 by the ratio $\beta_e(\lambda = 0.50)/\beta_s(\lambda = \lambda_1)$. This ratio was determined from Mie theory calculations of the wavelength dependence of β_s and β_e using the measured particle size distributions at the surface. $\lambda_1 = 0.475$ μm for the HSS visibility meter and 0.55 μm for the MRI integrating nephelometer. Although the HSS uses a light source at 0.88 μm, it was calibrated against a nephelometer operating at $\lambda = 0.475$ μm and is assumed to give β_s at 0.475 μm.

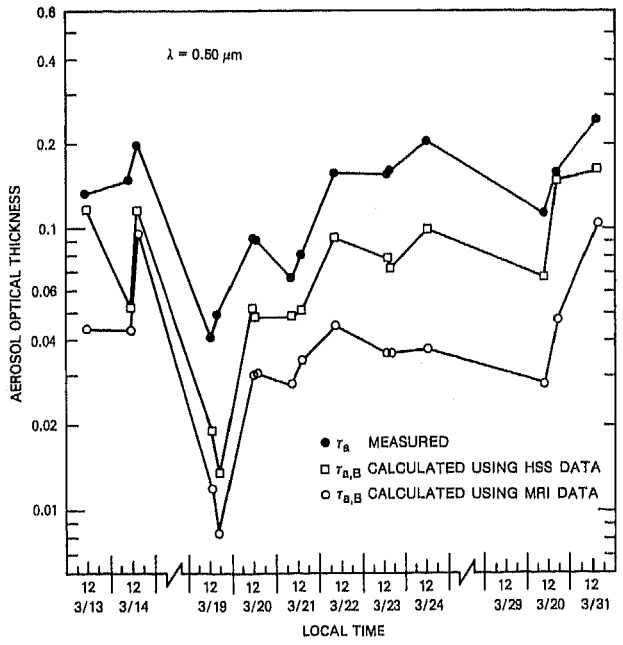

Fig. 36. Comparison of the spatial variations of the measured tropospheric aerosol optical thickness, τ_a, and the calculated optical thickness of the boundary layer, $\tau_{a,B}$, at a wavelength of 0.5 μm.

Values of $\tau_{a,B}$ were calculated for fourteen times between March 13 and 30 when the optical thickness was measured within about 1 hour of a radiosonde ascent. In addition, $\tau_{a,B}$ was calculated once each for March 30 and 31 when the elapsed time between the sun photometer measurement and the sounding was more than 2 hours.

Table 3 lists the times for which $\tau_{a,B}$ was calculated, the measured values of τ_a at these times, the time of the nearest sounding, the boundary layer heights, the calculated values of ζ, and the measured values of $\beta_s(z_0)$.

Figure 36 is a plot of the variation of τ_a and $\tau_{a,B}$ along the cruise track. It is seen that the measured and computed values of optical thickness track each other quite well. The correlation coefficient between τ_a and $\tau_{a,B}$ is 0.85 when HSS data are used to calculate $\tau_{a,B}$ and 0.82 when MRI data are used. The high correlation between τ_a and $\tau_{a,B}$ suggests that the spatial variation in the aerosol optical thickness of the troposphere over the subtropical Atlantic can be accounted for to a large degree by the combined effect of spatial variations in the depth, relative humidity, and aerosol characteristics of the boundary layer. Although there is a good correlation between the spatial variation of τ_a and $\tau_{a,B}$, there is a significant discrepancy in the absolute magnitude of computed and measured optical thicknesses. The measured value of τ_a is about twice the value of $\tau_{a,B}$ computed from the HSS scattering coefficients and 3–4 times the value

of $\tau_{a,B}$ computed from the MRI values of the scattering coefficient.

There are several possible explanations for the discrepancy between the measured and computed optical thicknesses. First, there may have been a significant contribution to the optical thickness from the region of the troposphere above the boundary layer. However, this contribution would have to be highly correlated with the boundary layer optical thickness in order to explain the good correlation between the measured optical thickness and the calculated optical thickness of the boundary layer. A second possibility is that we have underestimated the El Chichon stratospheric contribution. This contribution, however, is independent of the boundary layer conditions. The use of a higher value for the stratospheric contribution would likely result in a poorer correlation between the measured optical thickness and $\tau_{a,B}$. A third explanation for the discrepancy is the occurrence of systematic errors in the measured values of the aerosol scattering coefficient at the surface. Finally, the assumptions made in computing the profiles of aerosol extinction may also have contributed to the discrepancy between the measured and calculated optical thicknesses.

6. CONCLUSIONS

The measured size distributions presented in this report are, to our knowledge, the most extensive and accurate measurements of the size distribution of submicron particles in the marine environment to date. The size distributions were supplemented by measurements of aerosol scattering coefficient and optical depth, extensive meteorological observations, balloon soundings, satellite coverage, calculated air mass trajectories, and aerosol chemistry. This support made it possible to correlate changes in the size distribution with meteorological history, thus arriving at some unique interpretations of the mechanisms responsible for shaping the size distribution. Eight detailed case studies of the evolution in the size distributions which occurred under different meteorological conditions were presented and possible mechanisms responsible for the changes were discussed in sections 3 and 4. Some of the more important observations and conclusions are the following.

1. As an air mass moves off the continents in the absence of clouds or precipitation, there is a rapid decay of small particles ($r < 0.05$ μm) due to both coagulation and growth by condensation of nonvolatile gas-phase reaction products on the small particles. This creates a size distribution with a strong peak (accumulation mode) in the 0.05–0.08 μm radius range. The size distribution of these particles will often be modified by nonprecipitating clouds in the marine boundary layer before they are eventually removed by precipitation scavenging.

2. The cycling of aerosols through nonprecipitating clouds which are frequently present at the top of the marine boundary layer is a major factor in shaping the submicron aerosol size distribution. This cycling through clouds results in the repeated formation and evaporation of cloud droplets which form on the subset of particles called cloud condensation nuclei. During the cloud stage, trace gases are absorbed into the droplets where some are chemically converted into nonvolatile material which remains as part of the CCN after evaporation of the water. In addition, a significant fraction of the smaller interstitial particles are captured by the cloud droplets, causing a decrease in the particles too small to be CCN. These processes cause an increase in the mass of CCN and a minimum in the size distribution at the radius which separates interstitial and CCN portions of the size distribution.

3. The "background aerosol" found in the remote tropical MBL is not aged continental aerosol but is maintained by in situ formation of new particulate matter from the gas phase. (Particles larger than about 0.5 μm are, of course, largely sea-salt aerosol generated at the sea surface.)

4. To maintain the small size portion of the size distribution ($r < 0.05$ μm), there must be a source of small particles in the MBL. These particles are probably formed by heteromolecular homogeneous nucleation (or nucleation on cluster ions) at an average rate of the order of 10–100 particles cm^{-3} d^{-1} in the remote tropics. The exact chemistry of the nucleating species is unknown but undoubtedly involves gas-phase reaction products of very low volatility (such as H_2SO_4, MSA, and $(NH_4)_2SO_4$). These small particles subsequently grow by the condensation of additional gas-phase reaction products. There are known reaction pathways which lead from volatile gases of marine origin (such as DMS and H_2S) to species of low volatility.

5. A possible picture of the average life cycle of small marine particles in the remote tropics might be the following: New particles are formed at very small sizes at a rate on the order of 10–100 cm^{-3} d^{-1}, growing to about 0.04 μm in several days, at which time they become CCN and are cloud droplets during cloud cycles. On the average, they participate in 10–20 nonprecipitating cloud cycles over a 3–10 day period, growing to a size of about 0.1 μm before being removed by precipitation scavenging in a rain cloud.

The particle size distributions were used to calculate the aerosol scattering and extinction coefficients in the MBL and, together with soundings of relative humidity, were also used to calculate the aerosol optical depth of the marine boundary layer. An analysis and comparison of the measured and calculated optical properties leads to the following conclusions.

1. In general, measured and calculated values of the scattering coefficient track quite well. The calculated values are higher than the readings from the MRI integrating nephelometer but agree to within a factor of 2. The scattering coefficients measured with the HSS forward scattering instrument correlated well with both the MRI and calculated values, except for periods when the wavelength dependence of the scattering coefficient was significantly weaker or stronger than the average. This leads us to conclude that the accuracy of the HSS readings depends on the particle size distribution and that the HSS will overestimate or underestimate the scattering coefficient depending on whether the slope of the size distribution at the time is significantly flatter or steeper than the slope of the size distribution(s) used to obtain the instrument's primary calibration. Variations in the scattering coefficient along the ship's track can be explained by changes in meteorological conditions and air mass history. At low wind speeds, the scattering coefficient in air which has resided over the ocean for at least ten days is about 0.01 km^{-1}.

2. The calculated dependence of the aerosol extinction coefficient on wavelength ranged from weak to strong, depending on the relative concentration of large to small particles. The ratio of the extinction coefficient at 0.5 μm

wavelength to that at 8 μm ranged from 13.5 following 36 hours of wind speeds below 2.0 m s^{-1} to 1.5 following 4 days of wind speeds in the range of 7–12 m s^{-1}.

3. The contribution to the scattering coefficient at 0.55 μm from particles larger than 1.0 μm ranged from about 10 to 60%.

4. When the effects of relative humidity fluctuations on the variability of the scattering coefficient were removed by normalizing the values to a constant relative humidity, the scattering coefficients at visible and infrared wavelengths showed a significant dependence on wind speed. In the mean, the scattering coefficient at 0.5 μm wavelength increased by about a factor of 5 with an increase in the 12-hour average wind speed from 2 to 12 m s^{-1}. The calculated scattering coefficient at 5.0 μm increased by a factor of 10 over the same range of wind speed.

5. The measured values of tropospheric optical thickness ranged from 0.04 to 0.25 at a wavelength of 0.5 μm. The Angstrom power law, $\tau_a(\lambda) = \beta\lambda^{-\alpha}$, was used to describe the wavelength dependence of the aerosol optical thickness. The exponent α, which is directly related to the slope of the particle size distribution, was found to be higher near the east coast of the United States than over the remote areas of the Atlantic. The average values of α and β for the trans-Atlantic portion of the cruise were 1.03 and 0.075, respectively.

6. The optical thickness of the boundary layer was calculated from the value of the scattering coefficient at the surface and boundary layer height and relative humidity profile obtained from balloon soundings. It was assumed that the boundary layer was well-mixed and that aerosol concentrations were constant with height in the boundary layer. The optical thickness of the boundary layer was found to track the variation of the tropospheric optical thickness quite well, the correlation coefficient between the two being 0.85. This indicates that the spatial variation of the optical depth of the troposphere over the Atlantic Ocean can, to a large degree, be accounted for by variations in aerosol extinction in the boundary layer. This, of course, would not be true during episodes of Saharan dust transport. Although there was a high correlation between changes in the optical thickness of the troposphere over the ocean and changes in the optical thickness of the boundary layer, the troposphere optical thickness was a factor of about 2 higher than the boundary layer optical thickness if the HSS values of the scattering coefficient at the surface are used to calculate the latter and a factor of about 4 higher if the MRI scattering values are used. At present, it is difficult to explain how the measured and calculated optical thicknesses could be so highly correlated yet differ in magnitude by so much.

If the submicron particles are assumed to be of nearly uniform chemical composition, then there is a unique relationship between size and the critical supersaturation required to nucleate the particle. All of the size distributions given in this report have been converted to supersaturation spectra and are given by *Hoppel et al.* [1989].

Acknowledgments. This paper is dedicated to the memory of Eugene J. Mack (1942–1986) who died suddenly on October 18, 1986. Gene participated in the 1983 cruise reported here as well as in a number of prior research cruises sponsored by NRL. E. J. Mack was known to be a hard worker whose vast field experience had given him outstanding insight into meteorological processes. He was personable and cooperative and had a good sense of humor. He has been and will be sorely missed by his friends at NRL even as he is by his wife, his four children, and his colleagues at Calspan Corporation. We also would like to thank Roger Helvey for providing the balloon soundings which were extremely useful in establishing the depth of the marine boundary layer and the thickness of the stratus cloud decks when they were present and to Joyce Harris of NOAA for the trajectory analysis used to establish the history of the air mass encountered during the cruise. Partial support for this research was provided by ONR, Code 12 (Paul Twitchell).

REFERENCES

Andreae, M. O., and H. Raemdonck, Dimethylsulfide in the surface ocean and the marine atmosphere: A global view, *Science*, *221*, 744–747, 1983.

Andreae, M. O., R. Ferek, F. Bermond, K. P. Byrd, R. T. Engstrom, S. Hardin, P. D. Houmers, F. LeMarrec, and H. Raemdonck, Dimethylsulfide in the marine atmosphere, *J. Geophys. Res.*, *90*, 12,891–12,900, 1985.

Angstrom, A., The parameters of atmospheric turbidity, *Tellus*, *16*, 64–75, 1964.

Bates, T. S., J. D. Cline, R. H. Gammon, and S. R. Kelley-Hanson, Regional and seasonal variations in the flux of oceanic dimethylsulfide to the atmosphere, *J. Geophys. Res.*, *92*, 2930–2938, 1987.

Bigg, E. K., J. L. Gras, and C. Evans, Origin of Aitken particles in remote regions of the southern hemisphere, *J. Atmos. Chem.*, *1*, 203–214, 1984.

Bullrich, K., Scattered radiation in the atmosphere and the natural aerosol, *Adv. Geophys.*, *10*, 99–200, 1964.

d'Almeida, G. A., R. Jaenicke, P. Roggendorf, and D. Richter, New sunphotometer for network operation, *Appl. Opt.*, *22*, 3796–3801, 1983.

Dave, J. V., Subroutines for computing the parameters of electromagnetic radiation scattered by a sphere, *Rep. 320-3237*, IBM Palo Alto Sci. Cent., Palo Alto, Calif., 1968.

Dinger, J. E., H. B. Howell, and T. A. Wojciechowski, On the source and composition of cloud condensation nuclei in the subsident air mass over the North Atlantic, *J. Atmos. Sci.*, *27*, 791–797, 1970.

Elterman, L., UV, visible, and IR attenuation for altitudes to 50 km, *AFCRL Rep. 68-0153*, Air Force Cambridge Res. Lab., Bedford, Mass., 1968.

Fairall, C. W., and K. L. Davidson, Dynamics and modeling of aerosols in the marine atmospheric boundary layer, in *Oceanic Whitecaps*, edited by E. C. Monahan and G. MacNiocaill, pp. 195–208, D. Reidel, Hingham, Mass., 1986.

Fitzgerald, J. W., and W. A. Hoppel, Equilibrium size of atmospheric particles as a function of relative humidity: Calculations based on measured aerosol properties, in *Hygroscopic Aerosols*, edited by L. Ruhnke and A. Deepak, pp. 21–34, A. Deepak Publishing, Hampton, Va., 1984.

Frohlich, C., and G. E. Shaw, New determination of Rayleigh scattering in the terrestrial atmosphere, *Appl. Opt.*, *19*, 1773–1775, 1980.

Gathman, S. G., Optical properties of the marine aerosol as predicted by the Navy aerosol model, *Opt. Eng.*, *22*, 57–62, 1983.

Giorgi, F., A particle dry-deposition parameterization scheme for use in tracer transport models, *J. Geophys. Res.*, *91*, 9794–9806, 1986.

Hanel, G., The real part of the mean complex refractive index and the mean density of samples of atmospheric aerosol particles, *Tellus*, *20*, 371–379, 1968.

Hanel, G., The properties of atmospheric aerosol particles as functions of the relative humidity at thermodynamic equilibrium with the surrounding moist air, *Adv. Geophys.*, *19*, 77–188, 1976.

Hanel, G., and M. Lehmann, Equilibrium size of aerosol particles and relative humidity: New experimental data from various aerosol types and their treatment for cloud physics applications, *Contrib. Atmos. Phys.*, *54*, 57–71, 1981.

Harris, J. M., The GMCC atmospheric trajectory program, *NOAA Tech. Memo. ERL ARL-116*, Air Resour. Lab., Rockville, Md., 1982.

Hatakeyama, S., K. Izumi, and H. Akimoto, Yield of SO_2 and formation of aerosol in the photo-oxidation of DMS under atmospheric conditions, *Atmos. Environ.*, *19*, 135–141, 1985.

Hoppel, W. A., Growth of condensation nuclei by heteromolecular condensation, *J. Rech. Atmos.*, *9*, 167–180, 1975.

Hoppel, W. A., Nucleation in the MSA-water vapor system, *Atmos. Environ.*, *21*, 2703–2709, 1987.

Hoppel, W. A., and G. M. Frick, Ion-aerosol attachment coefficients and the steady-state charge distribution on aerosols in a bipolar ion environment, *Aerosol Sci. Technol.*, *5*, 1–21, 1986.

Hoppel, W. A., and G. M. Frick, The nonequilibrium character of the aerosol charge distribution produced by neutralizers, *Aerosol Sci. Technol.*, in press, 1990.

Hoppel, W. A., J. W. Fitzgerald, and R. E. Larson, Measurement of atmospheric aerosols: Experimental methods and results of measurements off the east coast of the United States, *Rep. 8703*, 66 pp., Nav. Res. Lab., Washington, D. C., 1983. (Available as ADA 130998 from Natl. Tech. Inf. Serv., Springfield, Va.)

Hoppel, W. A., R. E. Larson, and M. A. Vietti, Aerosol size distributions at a site on the east coast of the United States, *Atmos. Environ.*, *18*, 1613–1621, 1984.

Hoppel, W. A., J. W. Fitzgerald, and R. E. Larson, Aerosol size distributions in air masses advecting off the east coast of the United States, *J. Geophys. Res.*, *90*, 2365–2379, 1985.

Hoppel, W. A., G. M. Frick, and R. E. Larson, Effect of nonprecipitating clouds on the aerosol size distribution in the marine boundary layer, *Geophys. Res. Lett.*, *13*, 125–128, 1986.

Hoppel, W. A., J. W. Fitzgerald, G. M. Frick, R. E. Larson, and B. J. Wattle, Preliminary investigation of the role that DMS and cloud cycles play in the formation of the aerosol size distribution, *Rep. 9032*, ADA-185002), 33 pp., Nav. Res. Lab., Washington, D. C., 1987. (Available as ADA-185002 from Natl. Tech. Inf. Serv., Springfield, Va.)

Hoppel, W. A., J. W. Fitzgerald, G. M. Frick, R. E. Larson, and E. J. Mack, Atmospheric aerosol size distributions and optical properties found in the marine boundary layer over the Atlantic Ocean, *Rep. 9188*, 75 pp., Nav. Res. Lab., Washington D. C., 1989. (Available as ADA 210800 from Natl. Tech. Info. Serv., Springfield, Va.)

Hoyt, D. V., A redetermination of the Rayleigh optical depth and its application to selected solar radiation problems, *J. Appl. Meteorol.*, *16*, 432–436, 1977.

Larson, R. E., Measurement of radioactive aerosols using thin plastic scintillators, *Nucl. Instrum.*, *108*, 467–470, 1973.

Mack, E. J., B. J. Wattle, and C. W. Rogers, Fog characteristics at Otis AFB, Massachusetts, *Rep. 6655-M-1*, Arvin/Calspan Adv. Technol. Cent., Buffalo, N. Y., 1980.

Mack, E. J., C. W. Rogers, and B. J. Wattle, Marine aerosol characteristics in the subtropical North Atlantic and at North American coastal sites, *Rep. 6890-M-1*, Arvin/Calspan Adv. Technol. Cent., Buffalo, N. Y., 1986.

McCartney, E. J., *Optics of the Atmosphere*, 408 pp., John Wiley, New York, 1976.

Mirabel, P., and J. L. Katz, Binary homogeneous nucleation as a mechanism for the formation of aerosols, *J. Chem. Phys.*, *60*, 1138–1144, 1974.

Parungo, F., J. Harris, B. Rosenwasser, and L. Ruhnke, Analyses of aerosol and precipitation samples collected during a transatlantic research cruise, *NOAA Tech. Memo. ERL ESG-5*, 63 pp., Rockville, Md., 1984.

Pruppacher, H. R., The role of cloud physics in atmospheric multiphase systems: Ten basic statements, in *Chemistry of Multiphase Atmospheric Systems*, *NATO ASI Ser.*, vol. 6, edited by W. Jaeschke, pp. 133–190, Springer–Verlag, New York, 1986.

Reiss, H., The kinetics of phase transitions in binary systems, *J. Chem. Phys.*, *18*, 840–848, 1950.

Shettle, E. P., and R. W. Fenn, Models for the aerosols of the lower atmosphere and the effects of humidity variations on their optical properties, *AFGL Rep. TR-79-0214*, Air Force Geophys. Lab., Bedford, Mass., 1979.

Spinhirne, J. D., and M. D. King, Latitudinal variation of spectral optical thickness and columnar size distribution of the El Chichon aerosol layer, *J. Geophys. Res.*, *90*, 10,607–10,619, 1985.

Tomasi, C., and F. Prodi, Measurements of atmospheric turbidity and vertical mass loading of particulate matter in marine environments (Red Sea, Indian Ocean, Somalian Coast), *J. Geophys. Res.*, *87*, 1279–1286, 1982.

Twomey, S., On the composition of cloud nuclei in the northern United States, *J. Rech. Atmos.*, *3*, 281–285, 1968.

Young, T. A., On the Rayleigh-scatering optical depth of the atmosphere, *J. Appl. Meteorol.*, *20*, 328–330, 1981.

J. W. Fitzgerald, G. M. Frick, W. A. Hoppel, and R. E. Larson, Atmospheric Physics Branch, Space Sciences Division, Naval Research Laboratory, Washington, DC 20375.

(Received March 31, 1989;
revised July 25, 1989;
accepted September 15, 1989.)